Aalto University
School of Science
Master's Programme in Life Science Technologies,
Human Neuroscience and Technology

Emi Iizuka

Characterizing simultaneous multi-slice imaging with multifocal visual stimulation

Master's Thesis
Espoo, November 20, 2019

Supervisor: Professor Lauri Parkkonen

Advisors: D.Sc. (Tech.) Toni Auranen
(Staff Scientist, Aalto NeuroImaging)

D.Sc. (Tech.) Linda Henriksson
(University Lecturer, Aalto University)

Aalto University
School of Science
Master's Programme in Life Science Technologies,
Human Neuroscience and Technology

ABSTRACT OF
MASTER'S THESIS

Author: Emi Iizuka

Title:
Characterizing simultaneous multi-slice imaging with multifocal visual stimulation

Date: November 20, 2019 **Pages:** 73

Major: Human Neuroscience and Technology **Code:** SCI3601

Supervisor: Professor Lauri Parkkonen

Advisors: D.Sc. (Tech.) Toni Auranen
D.Sc. (Tech.) Linda Henriksson

Simultaneous multi-slice (SMS) echo-planar imaging (EPI) is an imaging technique that can be used to accelerate the imaging speed of a functional magnetic resonance imaging (fMRI) scan and increase the temporal resolution of the data acquisition. SMS EPI is already a widely evaluated imaging technique but its benefits for task-based fMRI are still unclear. The aim of this Thesis is to comprehensively characterise SMS EPI sequence using a multifocal stimulus paradigm. The multifocal fMRI mapping technique is a retinotopic mapping method that enables to map the activation cluster of multiple regions in a short time. The effects of preselected slice acceleration factors, fMRI paradigm repetition times (TR), flip angles and the use of generalized autocalibrating partially parallel acquisition (GRAPPA) acceleration are evaluated. In addition, the possibility to improve the multifocal fMRI mapping method with SMS EPI is examined.

The multifocal fMRI data were acquired with six different protocols. The repetition time (TR) of the reference protocol was 1800 ms. With different slice acceleration factors, the TR was shortened to be 900, 720, 400, 360 and 240 ms. Ten healthy subjects were measured with all six protocols. For half of the subjects, the flip angles were optimised with Ernst angle and for the others, the flip angle was chosen to be a constant 60 degrees.

The SMS EPI sequences were characterised by calculating local signal-to-noise ratios (SNR) and maximum t-statistics. Between protocols the achieved activation clusters (size and location) and multifocal maps were compared. Overall, shorter TRs increase statistical power, although a radical reduction of the TR decreases the SNR significantly. Even the TR of 240 ms results in reasonable data quality. The use of simultaneous GRAPPA acceleration has negative effects to the data quality, and optimised flip angles give significantly better outcomes than unoptimised flip angles. These results indicate that moderate slice acceleration factors have benefits to multifocal fMRI.

Keywords: functional magnetic resonance imaging, SMS EPI, BOLD fMRI, multifocal fMRI, retinotopic mapping

Language: English

Aalto-yliopisto
Perustieteiden korkeakoulu
Life Science Technologies

DIPLOMITYÖN
TIIVISTELMÄ

Tekijä:	Emi Iizuka		
Työn nimi:	Monileikekuvantamisen karakterisointi multifokaalisen näköärsykkeen avulla		
Päiväys:	20. marraskuu 2019	**Sivumäärä:**	73
Pääaine:	Human Neuroscience and Technology	**Koodi:**	SCI3601
Valvoja:	Professori Lauri Parkkonen		
Ohjaajat:	TkT Toni Auranen ja TkT Linda Henriksson		

Monileikekuvantaminen (SMS EPI) on kuvantamismenetelmä, joka mahdollistaa useamman leikkeen kuvantamisen samanaikaisesti ja siten lyhentää magneettikuvauksen kokonaisaikaa. Menetelmää on käytetty paljon erilaisissa tutkimuksissa, mutta sen mahdollisia hyötyjä ja haittoja tutkitaan edelleen. Tämän työn yhtenä tavoitteena on kokonaisvaltaisesti karakterisoida SMS EPI -sekvenssiä multifokaaliärsykkeen avulla. Käytetty multifokaalimenetelmä on retinotooppinen kartoitusmenetelmä, jonka avulla näköalueita kartoitetaan. Työssä tutkitaan, mikä vaikutus eri kiihdytyskertoimilla, käytetyllä toistoajalla (TR), flippikulman suuruudella ja mahdollisella GRAPPA-kiihdytyksellä on. Lisäksi tutkitaan, onko SMS EPI -sekvenssin avulla mahdollista parantaa jo valmiiksi optimoitua multifokaalimenetelmää.

Multifokaalidata kerättiin erilaisilla protokollilla, joissa käytetyt toistoajat lyhennettiin eri kiihdytyskertoimien avulla. Kiihdytyskertoimettoman vertailusekvenssin TR oli 1800 ms. Muissa protokollissa kiihdytyskertoimien avulla TR lyhennettiin 900, 720, 400, 360 ja 240 ms:iin. Kymmenen tervettä koehenkilöä mitattiin kaikilla protokollilla. Puolet koehenkilöistä mitattiin käyttäen Ernstin kulmalla optimoituja flippikulmia. Muiden koehenkilöiden kohdalla flippikulma asetettiin olemaan 60 astetta riippumatta käytetyistä protokollista. Eri SMS EPI -sekvenssit karakterisoitiin laskemalla paikallinen signaali-kohina suhde (SNR) ja t-testin t-arvoja. Lisäksi aktivaatioklustereiden kokoa ja sijaintia sekä saatuja multifokaalikarttoja verattiin protokollien välillä toisiinsa.

Kokonaisuudessaan työ osoittaa, että lyhyempi TR antaa tilastollista hyötyä, vaikka sen radikaalinen lyhentäminen selkeästi pienentää SNR:ää. Kuitenkin jopa 240 ms toistoajalla saatiin vielä luotettavia tuloksia. Lisäksi työ osoittaa, että optimoiduilla flippikulmilla on positiivinen vaikutus tuloksiin. GRAPPA-kiihdytyksen samanaikainen käyttö leikekiihdytyksen kanssa vaikuttaa dataan negatiivisesti. Työ osoittaakin, että kohtuullisesta kiihdytyskertoimesta on hyötyä näköalueiden multifokaalikartoitukselle toiminnallisen magneettikuvauksen (fMRI) avulla.

Asiasanat:	toiminnallinen magneettikuvaus, SMS EPI, BOLD fMRI, multifokaali fMRI, retinotopia
Kieli:	Englanti

Acknowledgements

My journey towards this Thesis began one and half year ago in May 2018 when I started as a summer employee in AMI-Centre. This was my first working opportunity as a research assistant and everything was so new, exciting and amazing. I have been privileged to be able to see closely how experiments are constructed and how research processes are made. My first project in AMI-Centre was my Special Assignment that created a great basis for this Master's Thesis.

I would like to thank my supervisor Professor Lauri Parkkonen and my advisors Toni Auranen and Linda Henriksson for their collaboration, great advises and support. I am grateful for my amazing co-workers at AMI-Centre for making my time so instructive. Especially thank you Toni Auranen for challenging me and for making all this possible and Marita Kattelus for being supportive and present in my measurements. I have learned so much about magnetic resonance imaging, making of a research process and even a lot of myself. Thank you all who have been a part of my journey. My whole time in AMI-Centre has been an incredible learning experience.

Thank you for my family and friends for their tremendous support, patience, belief and help. Without you I would not be here now. Finally, I am grateful for everyone who have contributed in my academic years and made it possible to combine university studies and competitive sports at the highest level.

Espoo, November 20, 2019

Emi Iizuka

Abbreviations and Acronyms

ACS	Autocalibration signal
AR(1)	First-order autoregressive
BOLD	Blood oxygenation level dependent
CAIPIRINHA	Controlled aliasing in parallel imaging results in higher acceleration
EPI	Echo-planar imaging
fMRI	Functional magnetic resonance imaging
FOV	Field of view
FWE	Family-wise error
GLM	General linear model
GRAPPA	Generalized autocalibrating partially parallel acquisitions
HRF	Hemodynamic response function
LGN	Lateral geniculate nucleus
mffMRI	Multifocal functional magnetic resonance imaging
MPRAGE	Magnetization prepared rapid gradient echo
NIfTI	Neuroimaging informatics technology initiative
NMR	Nuclear magnetic resonance
RFT	Random field theory
SMS	Simultaneous multi-slice
SNR	Signal-to-noise ratio
SPM	Statistical parametric mapping
TE	Echo time
TR	Repetition time
tSNR	Temporal signal-to-noise ratio
V1	Visual area 1

Contents

Chapter 1

Introduction

Functional magnetic resonance imaging (fMRI) is a variant of the magnetic resonance imaging (MRI) that is a well known non-invasive imaging technique used in medical and research context. It enables to investigate changes in brain function over time with high spatial resolution. Spatial accuracy in fMRI is millimeters [1, 2]. Temporal resolution of fMRI is rather poor and slow imaging is its weakness. Simultaneous multi-slice echo-planar imaging (SMS EPI) technique is one example of pulse sequences that can be used to accelerate imaging and increase temporal resolution [3]. SMS imaging enables to acquire several slices simultaneously and thus the increase in temporal resolution is directly proportional to the number of simultaneously acquired slices. In this Thesis, different SMS EPI sequences are characterized.

Previous studies have shown that SMS EPI protocols have benefits for resting-state studies [4, 5] but for task-based fMRI the picture is less clear. Blood oxygen level dependent (BOLD) fMRI [6–8], that was also used in this work, is the most commonly used fMRI method. BOLD fMRI measures metabolic and vascular events due to neuronal activation [6, 8]. Since the time scale of neural events is milliseconds and the time scale of measured metabolic and vascular events is seconds [1], it is difficult to observe temporal information completely. Even though, it is not possible to increase the time scale of metabolic events, an accelerated sampling rate may be beneficial for statistical methods [4, 9, 10] which are typically used to quantify BOLD effects. Thus, accelerated imaging methods such as the SMS EPI technique might increase BOLD sensitivity [9]. The aim of this work is to evaluate benefits and disadvantages of SMS EPI sequence in task-based BOLD fMRI using multifocal stimulus paradigm [11].

Multifocal fMRI (mffMRI) mapping technique, used in this work, is a retinotopic mapping method for fMRI developed by Vanni and colleagues [12] and further developed by Henriksson and colleagues [11]. MffMRI enables to

map activation clusters of 24 multifocal regions in a short time. The position accuracy and intensity of the activation clusters between imaging sequences can be compared. MffMRI is used to map visual field maps as a part of visual fMRI studies. Since the mffMRI mapping method is already well optimised, in this work my aim is to examine whether it is possible to improve the routinely used multifocal mapping method further with SMS EPI protocols. Is it possible to accelerate data acquisition and improve BOLD sensitivity with SMS EPI sequences? Does the increased sampling rate affect the data quality and is the quality better with some slice acceleration factors than others?

The multifocal fMRI data is acquired with six different protocols: a standard single-slice EPI protocol and five SMS EPI protocols with different acceleration factors. The repetition time (TR) of the protocols varies between 1800 and 240 ms. Repetition time is the time interval between successive excitation pulses. In this work, also the effects of flip angles and the use of simultaneous generalized autocalibrating partially parallel acquisition (GRAPPA) acceleration to SMS fMRI data are evaluated.

I will characterize and compare different SMS EPI sequences by calculating local signal-to-noise ratio (SNR) values and maximal t-statistics. I will compare cluster sizes, locations and values of maximal t-scores and achieved multifocal maps (polar angle and eccentricity) of different protocols.

Although this work consists of many tasks, the main aim is to characterize and comprehensively evaluate SMS EPI sequence with multifocal stimulus paradigm. This Thesis starts with the background information that are needed to understand the work. Next, I will cover the used materials, data acquisition and the applied data analysis methods. Then, the results are presented. Finally, I will discuss the whole process and present my conclusions of the results.

Chapter 2

Background

This chapter covers the needed background information to understand the work done in this Thesis. I will cover basics of the used imaging methods, function of the visual cortex of the human brain and the mffMRI mapping method.

2.1 Principles of Magnetic Resonance Imaging

MRI is based on a physical phenomenon called nuclear magnetic resonance (NMR) [13]. It utilizes a strong magnetic field, and the measured signal is modulated with radio frequency and gradient field operations according to the used imaging sequence. MRI technique enables both high-quality images of the whole human body and detailed structural images of specific tissues and organs.

The most abundant atom of the human body is a hydrogen atom (approximately 63%), which has a magnetic dipole moment [1, 2, 13]. Nuclei that posses the magnetic moment property interact with an external magnetic field B_0 and produce NMR signal [1, 13]. Without an external magnetic field, magnetic moments of nuclei are randomly oriented according to the thermodynamic laws. When a strong external magnetic field B_0 is applied slightly more than half of the magnetic moments align parallel to the field (while rest of the nucleons retain anti-parallel due thermodynamic energy) creating net magnetization. When the alignment is achieved the nuclei are excited with radio frequency pulses. This magnetic field B_1 is perpendicular to B_0 and disturbs the alignment by changing the orientation of precessing hydrogen nuclei. The extent of tilt between the direction of the external magnetic field and the transverse magnetization is also known as a flip angle

(see Subsection 2.1.1).

After the pulses, magnetic moments will gradually realign with the external magnetic field B_0. The process is known as relaxation and it depends on the properties of the imaged tissues [1, 2]. Different processes during relaxation are known as T_1 and T_2/T_2^* [1, 2]. Time constant T_1 describes the relaxation process related to the recovery of the net magnetization along the longitudinal direction (as spins return to the parallel or anti-parallel state). Time constant T_2 describes the relaxation process related to spin-spin interactions. Time constant T_2^* describes the relaxation process related to spin-spin interactions and local magnetic field inhomogeneities that cause changes in the spin precession frequency. In table 2.1 rough values of time constants T_1 and T_2 of brain tissues are presented at a field strength of 3 Tesla that was used in this study.

	T_1 (ms)	T_2 (ms)
Gray matter	$1470^{+}_{-}50$ [14]	$99^{+}_{-}7$ [15]
White matter	$1110^{+}_{-}45$ [14]	$69^{+}_{-}7$ [15]

Table 2.1: Approximate relaxation times of brain tissues at 3 T.

Differences of relaxation processes in different tissue types are the basis of image contrasts. In the relaxation process, hydrogen nuclei emit an NMR signal that can be measured with radio frequency receiver coils [1, 2]. Because hydrogen content varies in different tissue types, it is possible to distinguish them with these measured signals. In structural imaging, the most commonly used contrast is T_1-weighting. This image contrast utilizes that different tissue types have rather different T_1 values [1, 2]. Since different tissues distinguish efficiently from T_1-weighted images, T_1-weighted contrast was used in structural images of subjects' brain. T_2^*-weighted contrast imaging is sensitive to differences of magnetic susceptibility [1, 2]. It is commonly used in fMRI studies and also in the experiments performed in this Thesis.

2.1.1 Flip angle

Flip angle is the change in the precession angle of the net magnetization during a radio frequency excitation. It is affected by the shape of the used radio frequency pulse, inhomogeneities of the B_0 field and slice selection gradients [1, 16].

To achieve maximal signal intensity, it is important to use optimised flip

angle (α_E). According to Ernst and Anderson [17]

$$\alpha_E = \arccos\left(e^{-TR/T_1}\right), \tag{2.1}$$

where TR is the repetition time and T_1 is the time constant of the longitudinal relaxation. T1 value for gray matter is approximately 1470 ms in 3 Tesla [14]. Figure 2.1 illustrates the change of optimal flip angle as a function of TR: the shorter the TR, the smaller the optimal flip angle. If the flip angle is defined to be too big related to TR, nuclei do not have enough time to realign with external magnetic field between radio frequency pulses, and the maximal possible signal intensity is not achieved [17].

The choice of the flip angle also influences the image contrast [1, 18]. The Ernst angle provides the maximum signal intensity for a single tissue but does not maximize the contrast between different tissue types. Therefore, also the research question determines which would be the optimal flip angle to use. In this work, I used both a constant flip angle and optimal flip angles calculated with the Ernst equation to observe their effects to signal intensity in the used SMS EPI sequences. In the protocols, TRs varied between 1800 and 240 ms.

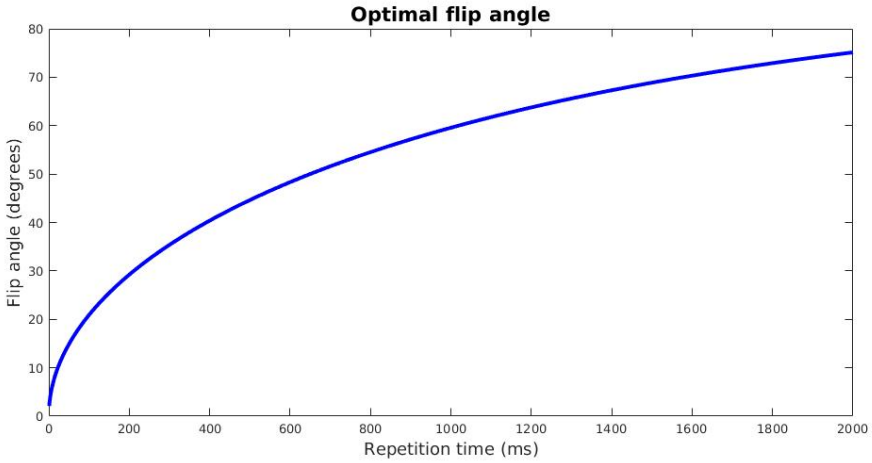

Figure 2.1: The optimal flip angle as a function of repetition time (TR) when T1 is 1470 ms. The shorter the TR is the smaller the optimal flip angle is. In this work, the TRs of evaluated SMS EPI sequences varied between 1800 and 240 ms.

2.1.2 Spatial encoding

The spatial information in the emitted signal is encoded with gradients [1]. Gradients with a low amplitude and a short duration encode low spatial frequencies. In that case, the gradients create a minimal wrap across the imaged object and only widely spaced objects are discriminated. Gradients with a high amplitude and a long duration instead encode high spatial frequencies. Hence, the amplitude and duration of the applied gradients together determine the final spatial frequency encoding.

Image acquisition can be considered using the concept of k-space that is a two dimensional matrix of spatial frequencies (kx, ky) of the raw MRI data. It is used to organize the gradient-derived spatial frequency information before the inverse Fourier transform and final image reconstruction. In a generic form,

$$\mathbf{k} = \gamma \int \mathbf{G}(t)dt, \tag{2.2}$$

where $\mathbf{G}(t)$ is a time-dependent gradient amplitude [19]. A diagram of k-space is illustrated in Figure 2.2. The central part of k-space contains low spatial frequencies while high spatial frequencies are encoded at the periphery of the k-space [19, 20]. In addition, the points in the center of k-space dominate the SNR, image contrast and are sensitive to motion artifacts. Points at outer part of k-space instead mainly delineate image details, noise in the image, maximum spatial resolution and produce less artifact from motion. The Fourier transformation of the k-space is the image.

The way how the various spatial frequencies are collected is known as the k-space trajectory and it varies between different pulse sequences. The simplest conventional method to map the k-space is to encode all the points of frequency direction (kx) line by line in each pulse cycle [19, 20]. Successive pulse cycles are separated by the TR. This standard k-space mapping method is very slow and used only in basic image sequences.

2.1.3 Echo-planar imaging sequence

In this work, I evaluated gradient single-shot echo-planar imaging (EPI) sequences that are widely used in functional imaging [1]. EPI is a fast MRI technique, which was first described by Mansfield in 1977 [21]. It has had a significant impact on the development of functional magnetic resonance imaging. The first EPI images of the human body were produced in 1983 when Mansfield's group imaged an infant human heart [22].

In EPI sequences the whole data of a particular slice are acquired after a single (or a small number of) radio frequency pulse using rapid gradient

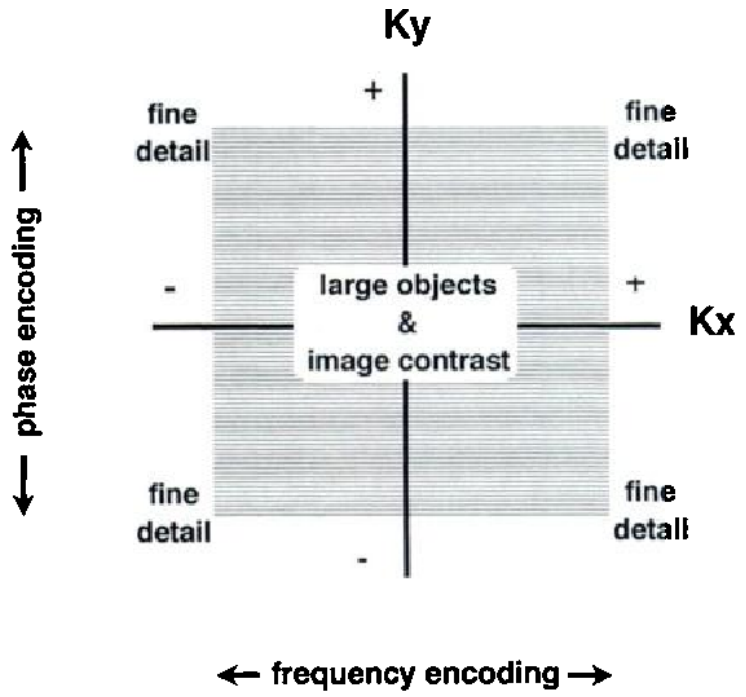

Figure 2.2: The diagram of k-space. High spatial frequencies (fine details and small objects) are encoded at the periphery and low spatial frequencies (large objects and image contrast) are encoded in the centre of the k-space. Frequency-encoding is along horizontal axis and phase-encoding along the vertical. The Fourier transformation of the k-space is the image. The diagram is adapted from Ref. [20].

switching [1, 20, 23]. Within one pulse cycle, the whole k-space is filled by back and forth trajectory where the alternating lines are scanned in opposite direction. This switchback approach requires a very strong gradient system since different sets of gradients must be cycled on to enable the 90° turns after each filled read-out lines [1, 20, 23]. A short phase-encoding gradient pulse is used to move the collection into the next line in the phase-encoding direction after each successively collected read-out lines. The EPI pulse sequence and its k-space trajectory are illustrated in Figure 2.3.

There are different variations of the EPI sequence but the main idea is the same for all of them [23]. For example, in the single-shot EPI, all k-space data are acquired within one pulse cycle. In multi-shot EPI, the data are collected with the same zig-zag trajectory but with a small number of radio frequency pulses. Within one pulse cycle only a part of the k-space data is

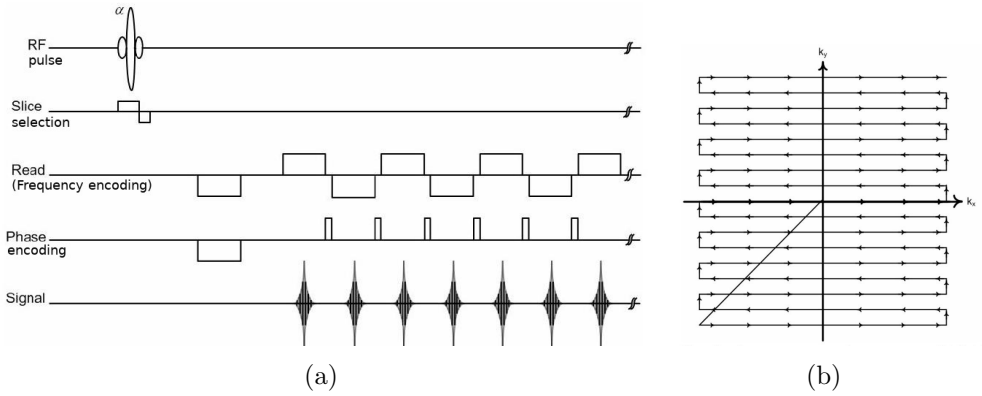

(a) (b)

Figure 2.3: EPI sequence (a) and corresponding collection of k-space trajectory (b). Slice selection, phase- and frequency-encoding indicate gradient operations. In (b) frequency-encoding is along horizontal axis and phase-encoding is along the vertical. Phase-encoding steps are filled with zig-zag trajectory. The Figure is modified from Ref. [24].

acquired and pulse cycles are repeated until full data is collected.

EPI technique is the most common imaging method for functional MRI due to the short image acquisition time [1, 19, 20, 23]. The fast acquisition time decreases the motion sensitivity and enables to image also the faster changing physiological changes [1, 19, 20, 23]. On the other hand, the fast EPI image requires greater gradient amplitudes to encode the signal and therefore the gradient system can become the limitation for faster imaging. A disadvantage of EPI method is its sensitivity to shape distortions and susceptibility artifacts [23].

2.2 Functional Magnetic Resonance Imaging

Where MRI provides a structural image of brain, fMRI enables us to investigate changes in brain function over time. A single functional image does not give any information of brain activity but examining changes across functional images over time does. Hence, in fMRI repeatedly sampled 3-D volumes of brain are formed to a time series of brain images during a task.

The critical factors to estimate the reliability of fMRI in research aspects are signal specificity and temporal and spatial resolution [2]. Signal specificity ensures that the measured signals reflect actual neural changes. Temporal resolution determines the time course of various neural events and spatial resolution delineates our capability to discern varieties in an image across

different spatial locations. Since the time scale of neural events is faster than the time scale of metabolic and vascular events which are measured in fMRI, some temporal information is difficult observe. SMS EPI sequences, which are characterized in this Thesis, can be used to improve temporal resolution. However, an open question is how much increased temporal resolution benefits since hemodynamic changes are slow.

The spatial resolution of fMRI is very good compared to other non-invasive functional imaging methods [1]. Even a very brief neuronal event cause physiological changes in an activation area and thus emits signals that are measured with fMRI. Spatial resolution of fMRI can be improved for example with an increased strength of magnetic field and use of optimised pulse sequences [2].

2.2.1 BOLD signal

Functional magnetic resonance imaging is based on measuring hemodynamic changes in the brain. BOLD imaging, which is based on the changes of blood oxygenation level during brain activation, is the most commonly used fMRI method. The phenomenon was discovered by Seiji Ogawa [6, 7] and Kwong with colleagues [8] and it is also applied in this study.

The activity of neurons increases their metabolic requirements. Since brain does not store energy, it must be provided continuously from the blood supply of the brain. The primary energy sources are glucose and oxygen [1]. The main oxygen carriers in blood are hemoglobin molecules, that have different magnetic properties whether or not oxygen is bounded to them. Oxygenated hemoglobin is diamagnetic while deoxygenated hemoglobin is paramagnetic [1, 2]. Diamagnetic molecules do not have a magnetic moment but paramagnetic molecules have. Hence, a change in hemoglobin oxygenation level changes the local magnetic susceptibility. Fully oxygenated blood has approximately the same magnetic susceptibility than other surrounding brain tissues while the fully deoxygenated blood does not [2]. Thus, deoxygenated blood induces some magnetic field distortions in an external magnetic field. Due to distortion, the local MRI signal decreases. An increase of neural activation causes an increase in the blood oxygenation level. And this effect finally increases the BOLD signal.

Since the BOLD signal is not an absolute measure of the neuronal activation, we are interested in the temporal changes of it rather than its absolute value. The change of the BOLD signal is characterized by hemodynamic response function (HRF) which is illustrated in Figure 2.4. Hemodynamic response results from a decrease in the concentration of deoxygenated hemoglobin present within a voxel. After a sensory stimulus, cortical neural

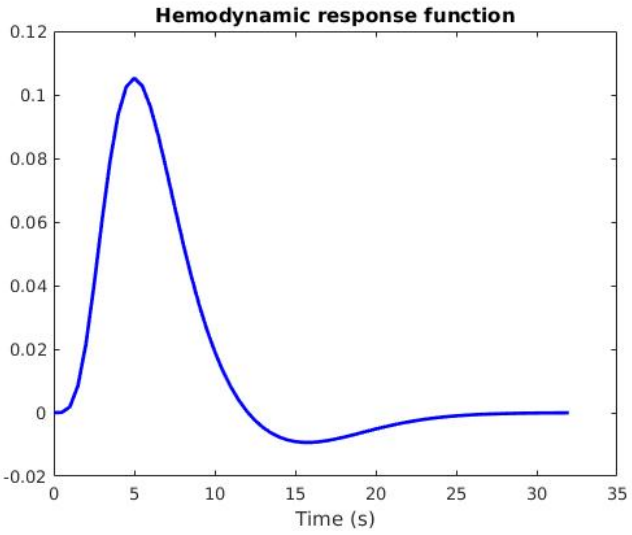

Figure 2.4: Model of hemodynamic response function (HRF). Here the peak is reached after 5 s.

responses occur within tens of milliseconds but the first observable changes of hemodynamic response occur only within 2 seconds. The maximum value of BOLD signal, which is known as the peak of the HRF, is reached around 5 to 10 seconds after start of neural responses [25, 26]. After reaching the peak, the cessation of neural activity decreases the amount of oxygenated hemoglobin and also the BOLD signal to a below-baseline level. This effect is known as the post-stimulus undershoot.

Because of the delay between neuronal and hemodynamic responses, it is challenging to study fast activation changes with BOLD fMRI. Another challenge is the variation in shape of the HRF between different individuals, brain regions and also for the same subject and brain region if the pre-scan conditions vary [25]. However, in visual cortex we can assume that HRF is same for all subjects.

2.3 Methods to accelerate data acquisition

A slow scanning speed is one weakness of fMRI and over the years researchers have studied methods to accelerate the data acquisition. In this section, I will introduce a partial Fourier technique and the development from standard parallel imaging to simultaneous multi-slice EPI imaging evaluated in this study.

2.3.1 Partial Fourier

Partial Fourier imaging techniques are reconstruction methods that use only one half of the k-space to generate a whole image. Since a time-domain echo signal is symmetric around its peak, the k-space has a mirrored property also known as conjugate (or Hermitian symmetry) [27]. Due to conjugate symmetry, points that are located diagonally from each other across the origin of the k-space can be calculated if the data of one of them is known [27]. For example, in Figure 2.5, if the data at R is the complex number $(a + bi)$ the data at D is R's complex conjugate $(a - bi)$. Hence, the points have identical amplitudes but opposite phases. The partial Fourier methods utilize this symmetry.

In theory, with partial Fourier technique a whole image can be generated with one half of a k-space which reduce the imaging time to the half [27]. However, the data set of image contain always some phase errors and therefore the approximation of the conjugate symmetry is not perfect. For example, in EPI, echoes that are acquired late after the radio frequency pulses will have different phase than early ones which will cause additional phase

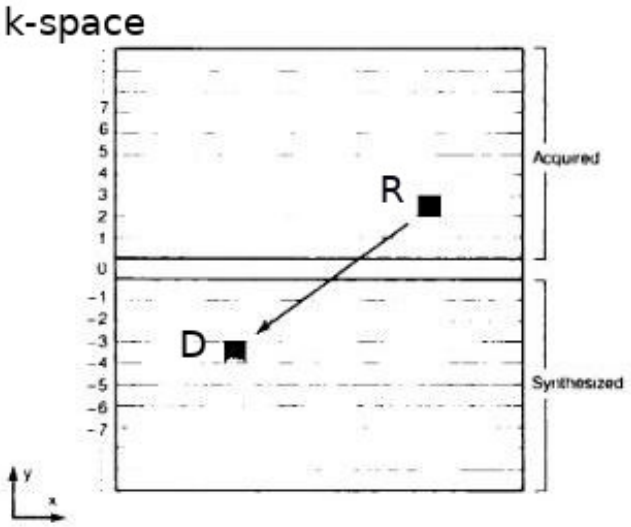

Figure 2.5: Conjugate symmetry of the points R and D. Due the mirrored property of the k-space, if the data for the point R are known, the data of the D can be calculated and vice versa. The point D is R's conjugate. In the partial Fourier reconstruction method only one half of the k-space (e.g the top part) is sampled and other half (e.g the bottom part) is synthesized/reconstructed. The image is modified from Ref. [27].

errors. Because of this with in partial Fourier of EPI sequences 6/8 or 7/8 of the k-space must be sampled to ensure accurate estimation of remaining portion [28].

Two major partial Fourier methods are phase conjugate symmetry and read conjugate symmetry. In the first one the direction of symmetry is the phase-encoding direction and in the later one the direction of symmetry is in the read out (frequency encoding direction). Read conjugate symmetry samples only part of the echo time (TE) that enables to use shorter TE values than would otherwise be possible. TE is the time interval between an excitation pulse and data acquisition. Read conjugate symmetry is especially useful for EPI [28]. Partial Fourier technique enables the same image contrast and spatial resolution but reduces SNR [27].

2.3.2 Parallel imaging

During the last 15 years, parallel imaging methods have been a widely studied research topic and nowadays there are several different parallel imaging reconstruction techniques and strategies. Standard parallel imaging methods accelerate the data acquisition time by reducing the number of space encoding steps (e.g. skipping every other phase-encoding line) with respective reconstruction methods [29]. These undersampled k-spaces lead to aliased images that reconstruction algorithms try to compensate. The algorithms reconstruct artifact-free images from either already formed aliased images (sensitivity encoding (SENSE)) [30] or from the undersampled data before the Fourier transformation (Gneralized autocalibrating partially parallel acquisition (GRAPPA)) [31]. Since we used the GRAPPA-type reconstruction in some of our data acquisition, I will cover GRAPPA in detail.

GRAPPA is a multi-coil parallel imaging technique introduced by Griswold and colleagues [31]. In general, parallel imaging methods such as GRAPPA utilize the technique where known placement and sensitivities of receiver coils are used to partially replace the spatial information of MRI signal which are normally completely encoded with switching gradients [32, 33]. The full process of GRAPPA can be divided into four major steps: data acquisition, estimation of missing k-space lines, generation of individual coil images and combining the single coil images.

In data acquisition, GRAPPA samples only a limited number of phase-encoding steps but the lines through the centre of k-space are fully sampled. These additionally acquired autocalibration signal (ACS) lines are used to estimate the sensitivities of receiver coils and they serve as a form of navigator measurements to missing k-space estimations [32, 33]. Missing k-space lines are estimated in an iterative way and estimation of k-space lines is done

separately to all coils [31].

After all uncombined individual coil images are obtained, they are combined into the final magnitude image using any array combination methods such as a sum of square reconstruction method [31, 32]. This magnitude reconstruction method eliminates signal losses due to phase cancellation and also improves SNR compared to other parallel imaging methods [32]. In addition, the GRAPPA algorithm is not affected by localized inhomogeneities and image distortions [32].

The GRAPPA is a very much used method in fMRI studies to accelerate scan time and to reduce susceptibility artifacts. However, there are also studies that show negative effects of it. For example Lutke and colleagues demonstrate that the combination of EPI and GRAPPA at reduction factor 2 has a small cost on BOLD fMRI sensitivity [34]. Especially if the calculation of missing k-space lines is inaccurate there will be aliasing artifacts in the reconstructed image, which can bee seen in the final obtained magnitude image [32]. In this study, I investigated the effects of GRAPPA on BOLD fMRI when using the SMS EPI sequences.

2.3.3 Simultaneous multi-slice imaging

Simultaneous multi-slice imaging uses parallel imaging combined with complex multiband radio frequency pulses to acquire several slices simultaneously [35]. This imaging method reduces significantly the data acquisition time since the reduction is directly proportional to the number of simultaneously excited slices.

As discussed in Subsection 2.3.2, reconstruction methods of standard parallel imaging take into account the spatial sensitivity information, provided by a multi-coil receiver array. Therefore, they are dependent on the geometry of the coil array when the slices that have essentially identical coil sensitivity profiles (e.g closely spaced slices) can not be separated or they suffer from an SNR reduction [29, 36]. To avoid these limitations Breuer and colleagues presented a technique termed 'Controlled aliasing in parallel imaging results in higher acceleration' (CAIPIRINHA) for multi-slice imaging [36]. Unlike standard parallel imaging postprocessing algorithms, this technique modifies the appearance of aliasing artifacts during the data acquisition and thus reduces dependence on the coil array geometry.

Normally simultaneously excited slices end up to be superimposed but in CAIPIRINHA technique these slices are shifted with respect to each other [36]. Shifting enables more variations in coil sensitivity profiles since parallel imaging reconstructions can exploit sensitivity variations in both slice- and phase-encoding directions. Hence, compared to conventional multi-

slice imaging, CAIPIRINHA technique enables better reconstructions which results better image quality, improved SNR and possibility to use higher acceleration factors [36].

In CAIPIRINHA, inter-slice shifts are controlled by using special phase modulated multi-slice radio frequency pulses. For example, to shift the image by a single pixel ($\Delta y = FOV/N$), one needs a linearly decreasing phase that runs from ($+\pi$) to ($-\pi$). The additional phase modulation of radio frequency pulses is then $\Theta_m = im2\pi/N$. N relates to the number of equidistantly sampled k-space points and index m is the actual encoding step. As a concrete example, in a simultaneous two-slice excitation the additional phase modulation is applied only to slice 2 which results in image $p(y)$ composed of two superimposed slices p_1 and p_2 that are shifted with respect to each other by the shift Δy. This can be expressed as

$$p(y) = \sum_{m=-N/2}^{N/2-1} (S_1(m\Delta k) + S_2(m\Delta k)e^{im\Delta k\Delta y})e^{im\Delta ky} = p_1 + p_2(y - \Delta y), \quad (2.3)$$

where $S(m\Delta k)$ indicates the k-space signal. [36] Figure 2.6 illustrates this simple simultaneous two-slice experiment (a) without and (b) with phase modulation. In general, CAIPIRINHA technique can be used to shift several simultaneous excited slices by shifting each slice independently with an arbitrary amount in the field of view (FOV). The CAIPIRINHA technique is possible to use for multi-shot acquisitions but not, for example, for single-shot EPI where only a single radio frequency pulse is used to acquire all k-spaces.

2.3.4 Simultaneous multi-slice echo-planar imaging

Since 1980 SMS imaging has been used to improve the efficiency of line-scan imaging techniques [37]. However, only after the SMS was adapted for the EPI sequence, the imaging method had a major impact in fMRI and diffusion MRI. Setsompop and colleagues presented the invention of blipped-CAIPIRINHA that brought the benefits of CAIPIRINHA also to single-shot EPI [3]. This technique was used in the experiments of this study to acquire multiple slices simultaneously.

Blipped-CAIPIRINHA is based on a Wideband-like technique introduced by Nunes and colleagues [38]. Blipped-CAIPIRINHA uses additional slice axis gradient (G_z) blips simultaneous with the EPI phase-encoding blips to induce inter-slice shifts. Additional gradient blips alternate from positive to negative to avoid accumulation of through-slice phase variation, which causes voxel tilting artifacts [3, 39].

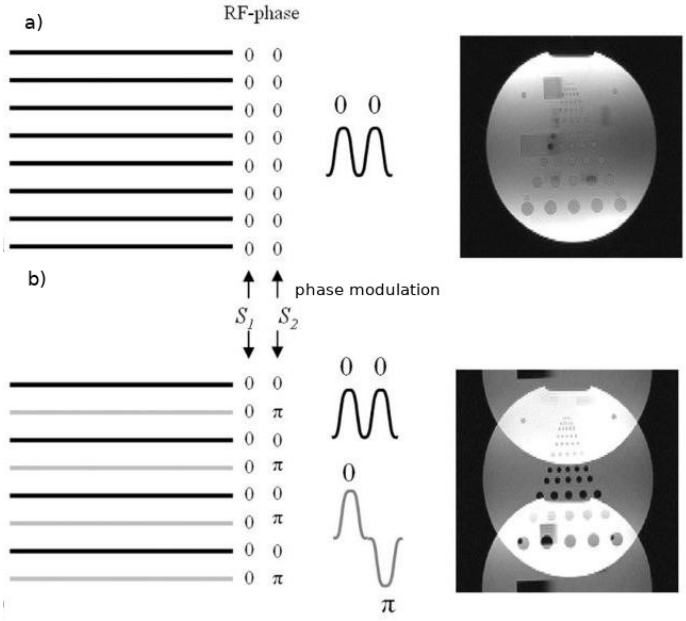

Figure 2.6: Schematic description of a simultaneous two-slice excitation of phantom a) without phase modulation and b) with phase modulation. After Fourier transformation the data acquired without any phase modulation produce totally overlapped slices (see image a) right). In the CAIPIRINHA technique, superimposed slices are sifted with respect to each other using phase modulation. This is illustrated in b) where the superimposed slices are shifted by FOV/2. The k-spaces of both situations are shown in the left. In the black k-space lines the phase has been same for both slices (0, 0) and in the gray k-space lines the phases have been different for both slices (0, π). The image is modulated from Ref. [36].

To create inter-slice shifts between the simultaneously excited slices for the data acquisition of each k-space line, additional G_z blips are applied concurrently with the phase-encoding blips (G_y) [3]. Figure 2.7 shows an example where the G_z blips are applied to create a FOV/2 shift between two simultaneously excited slices. The phase modulation caused by G_z blips are shown in Figure 2.7d. In the example, the additional gradient blips create a π phase modulation to the upper slice (blue) but not to the lower slice (red). This linear phase modulation along k_y causes the desired FOV/2 inter-slice shift along the phase-encoded direction. Each G_z blip causes also a small through-slice phase variation (2σ) (Figure 2.7a) which results in a very minor signal attenuation (usually less than 1%) [3, 39].

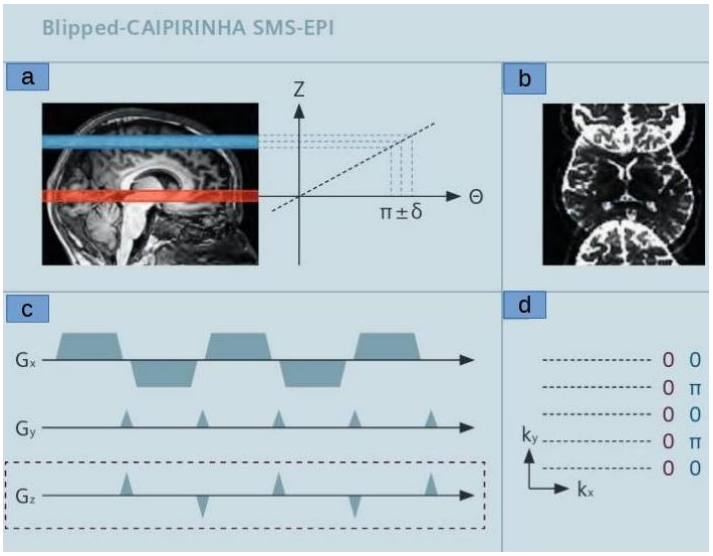

Figure 2.7: Example of the blipped-CAIPIRINHA SMS-EPI with two simultaneously excited slices. Blue and red slices (a) are excited simultaneously and FOV/2 inter-slice shift is created with additional gradient (G_z) blips (c). b) is the image after Fourier transformation and the phase modulation is illustrated in d). In every other k-space lines the phase is same for both slices (0, 0) and in the rest k-space lines the phases are different for both slices (0, π). G_z blips cause also through-slice phase variation (2σ) that is illustrated in a). The image is adapted from Ref. [39]

2.3.5 Properties of SMS EPI

SMS EPI imaging increases temporal resolution directly proportional to the number of simultaneously acquired slices [3]. Acquiring two slices simultaneously allows to double the number of slices to be acquired in the same TR or halves the TR used to sample the same amount of slices. Hence, SMS EPI protocols enable shorter TRs or thinner slices. In previous studies, slice acceleration factors up to 8-10 have been tested in 3 Tesla magnetic field [40, 41]. These protocols significantly reduced TR and provide high sampling rate. The shortest TR used in the studies has been 260 ms [40] while in this work, the TR is reduced to be 240 ms.

The using high slice acceleration factors may produce SNR reduction [9, 42, 43], cause slice leakage artifacts [9] and increase g-factor penalty [3]. g-factor delineates how well aliased pixels can be separated. False positive activation might appear when activation of one slice leaks into other simultaneously excited slices even though this is controlled with different recon-

struction techniques [9, 10]. Hence, using SMS EPI protocols is balancing between the benefits of temporal resolution and possible disadvantages of higher acceleration factors.

In fMRI, hemodynamic changes that have relative low frequency signal are imaged. Therefore, it may seem that higher temporal resolution provides only minor benefits. However, BOLD effects, which are usually imaged in fMRI, are quantified with statistical methods and these statistical tests depend significantly on the number of data points. Higher temporal resolution increases statistical power and thus produces benefits in statistical methods [4, 9, 10]. With SMS EPI protocols it is possible to increase data points or to achieve the same number of data points in a shorter data acquisition time.

All in all, benefits of SMS EPI protocols depend on the research questions. Xu and colleagues showed that slice acceleration factor up to 8 can be routinely used in fMRI [41] while Todd and colleagues demonstrated that already a slice acceleration factor 4 increases the number of false positives [9]. The optimal slice acceleration factor is region dependent [43]. In this work, I aimed to evaluate the benefits SMS EPI sequences have for using multifocal visual stimulation fMRI.

2.4 Visual system

2.4.1 Visual pathway

The processing of visual information begins in the retina which is the neuronal portion of the eye [44]. The retina consists of five types of neurons: photoreceptors, biopolar cells, ganglion cells, horizontal cells and amacrine cells. In the retina of a human eye, there are two types of photoreceptors, rods and cones, that are specialized for different aspect of vision [44]. Rods are very sensitive to light but have very low spatial resolution. Cones instead have high spatial resolution and are less sensitive to the light. They also enable us to see colors. Cones are responsible for our vision in daylight and are mainly placed in the central of retina, an area called fovea, where the best visual acuity is [44]. Towards the peripheral of the retina the density of cones reduces which also drops the visual acuity [45].

The information processing of human visual system starts from photoreceptors were light is converted into electrical signals. These action potentials travel then through the multilayered complex circuity of retinal intraneurons and finally to the brain via axon neurons of the optic nerve. The largest axons of the ganglion cells form the optic nerve and part of these axons cross

in the optic chiasm. Hence, the early visual cortex of both hemispheres receive information from both eyes. After the optic chiasm, the axons form optic tracts in which the visual information is transferred to lateral geniculate nucleus (LGN) of thalamus. From there the visual stimulus is projected to visual area 1 (V1). [44] LGN is the main link between the retina and the visual cortex [46]. The primary visual pathway is illustrated in Figure 2.8.

Once the visual signals reach the primary visual cortex, different kind of basic information about the orientation, motion, edges, depth and colors of objects in the visual field are extracted [44]. The neurons of V1 can be divided into simple and complex cells. Simple cells are more sensitive to the length of a bar-shaped moving light and complex cells are more sensitive to the direction of the moving light and the orientation of a boundary between shadow and light [44]. In human brain, cortex that is predominantly related to visual processing, covers approximately 25% of the total extent of cerebral cortex [44]. The estimated surface area of V1 is 2.2% of cerebral cortex [48]. From the primary visual cortex the information is conveyed through two pathways to higher-level visual areas where the visual signals are further processed.

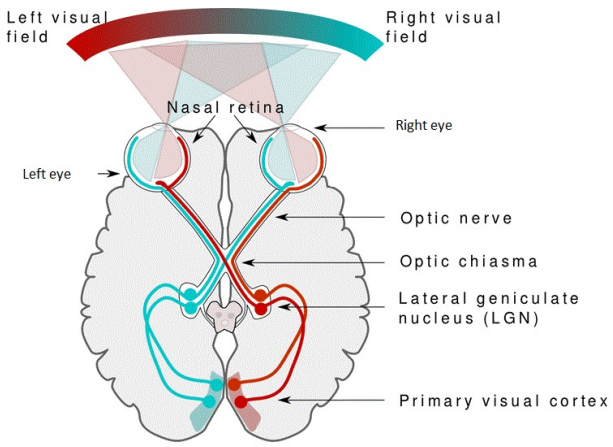

Figure 2.8: Pathway from the retina to the visual cortex. The visual information processing starts from the photoreceptors of the retina from where the information travel via axon neurons of the optic nerve. Part of the axons cross in the optic chiasm and thus the primary visual cortex of both hemispheres receive information from both eyes. After the optic chiasm the visual information is transferred to LGN which is the main link between the retina and the visual cortex. The image is adapted from Ref. [47].

2.4.2 Retinotopy

Retinotopy describes the spatial organization of the neuronal responses to visual stimuli. The primary visual cortex is retinotopically arranged. Each part of V1 receives information from a certain location of the visual field so that neighbouring cells respond to neighbouring parts in the visual field [44]. The average size of the receptive field increases as a function of the eccentricity of visual field [49]. The topographic representation of V1 is called a visual field map or a retinotopic map.

Retinotopic organization of the visual field in V1 is illustrated in Figure 2.9. In V1, the vertical meridian of the visual field runs approximately along the borders of V1 and horizontal meridian along the calcarine sulcus. The fovea is represented in the occipital pole while the periphery of the visual field is represented more anteriorly. The upper part of the visual field is mapped below the calcarine sulcus and the lower part of the visual field above it. There is also retinotopic organization in many other visual areas such as in visual areas V2, V3 and hV4 [50, 51]. Retinotopic organizations of human visual cortex can be mapped with fMRI.

2.4.3 Multifocal fMRI

Multifocal fMRI (mffMRI) mapping technique is a retinotopic mapping method for functional MRI developed by Vanni and colleagues [12] and further developed by Henriksson and colleagues 2012 [11]. It enables to assess a large number of visual field regions in a reasonable measurement time with excellent spatial resolution. Compared to a travelling wave method [50, 52], which is another way to map the retinotopic organization, the mffMRI method stimulates discrete regions of the visual field instead of continuous areas simulated with moving flickering checker board stimuli. The discrete stimulation enables the center of the mass of activated cortex for each region to be reliably delineated and thus results correspond better to retinotopic representation [12].

Other benefits of the mffMRI mapping is its straightforwardness which increases mapping accuracy. The mffMRI applies an analysis method based on standard general linear model (GLM) [12]. In practise, this enables quite automatic retinotopic mapping in 3D with all standard fMRI analysis software with minimum assumptions. Hence, the mffMRI method can be used as a part of different visual experiments as a routine way to map visual field maps.

The mffMRI method can only be used to map the retinotopic areas because signals from nonretinotopic areas correlate with each other which make

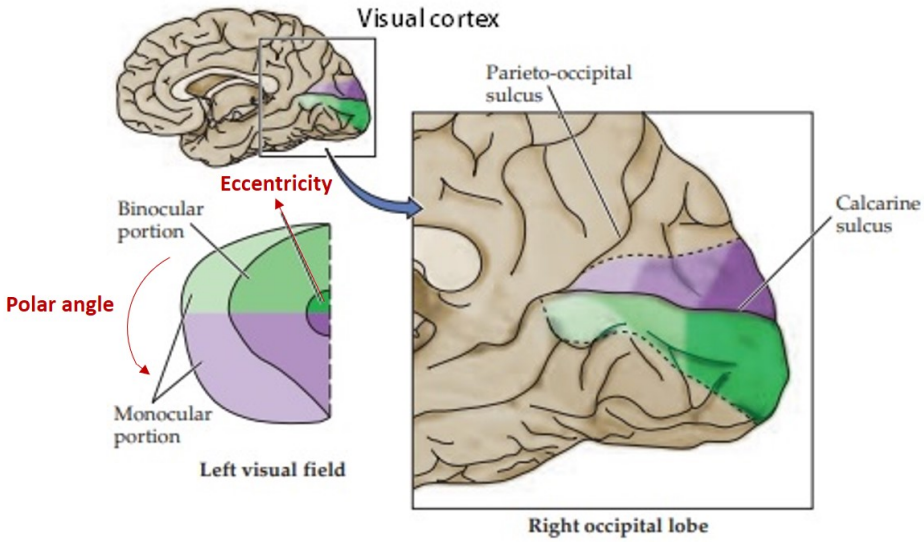

Figure 2.9: Retinotopy of visual cortex. The left side of the visual field activates more the right side of the visual cortex and vise versa. The border between green and violet colors illustrates the horizontal meridian of the visual field that runs along the calcarine sulcus. Stimulus above the horizontal meridian activates the brain below the calcarine sulcus and stimulus below the horizontal meridian activates the brain above the calcarine sulcus. Eccentricity of visual field is illustrates with hue. The center of visual field is represented in the occipital pole while the periphery of the visual field is represented more anteriorly. The monocular portion is an area that is only seen with one eye and the binocular portion is an area seen with both eyes. The image is modified from Ref. [44].

it difficult to identify them from the multifocal data. Stimulated regions of visual field should be large enough to evoke detectable signals. There are for example evidence that the mffMRI method works well to V1 area when the visual field is divided to 60 [12] or 24 regions [11].

Although, the standard mffMRI method enables to map multiple local visual field representations in a reasonable time, I was interested to know could it be even faster. In this experiment I aimed to improve the mffMRI method by applying SMS EPI sequences in the data acquisition which would increase mapping accuracy and/or decrease the total measurement time.

Chapter 3

Research materials and methods

This chapter covers the research methods used in this Thesis and detailed information on the data acquisition. The main part of the Thesis was to acquire multifocal fMRI data that can be used to comprehensively compare standard and SMS EPI sequences. The full study consisted of an fMRI imaging session where the same multifocal visual stimulus was measured with different protocols using different slice acceleration factors. I used the multifocal mapping method (stimuli and data analyses) as described by Henriksson and colleagues [11].

3.1 Stimuli and experimental design

I used a 24-region multifocal checkerboard stimulus introduced by Henriksson and colleagues [11]. The stimulus is routinely used for retinotopic mapping of the human visual cortex. It is optimised for visual areas V1, V2 and V3 but typically also quite good for visual areas hV4 and V3AB. The following introduction of the multifocal stimulus will be based on Henriksson and colleagues [11].

The visual field is divided into 24 regions, in 3 rings and 8 wedges. In our current setup, the three rings are divided so that the first ring covers 0.5–2.3 degree radius, the second ring 2.3–4.7 degree radius and the third ring 4.7–8.4 degree radius. The regions are simulated with a high contrast checkerboard pattern using temporally orthogonal stimulus sequences to produce temporally orthogonal time series of each region (for details on the sequences used to produce these time series see Vanni and colleagues [12]). Figure 3.1 illustrates the stimulus and how the visual field is divided into multifocal regions. There are no prior limitations due to the multifocal method for the number of simulated regions or to the size of the visual field [11].

One experimental run consists of 33 miniblocks with no simulation in first and last blocks. In one miniblock approximately half of the stimulus regions (10–15) are stimulated in two sets to minimize the effects of nonlinearities in spatial summation. The sets are formed so that the regions sharing the same border are not simulated at the same time. In the middle of the stimulus there is a fixation dot which subjects were asked to passively look at.

During a miniblock the first set of regions is on 115 ms and 115 ms in two opposite contrasts and then for 135 ms the checkerboard pattern disappears. After this a second set of regions is displayed. One miniblock lasts 7.2 seconds and during it two sets of stimulus regions are shown multiple times. The total time of one multifocal run is about 4 minutes. To get enough variation into the measured signals, the stimulated regions are simulated in two temporally different multifocal runs. For more information of the stimuli, see Henriksson and colleagues [11].

The stimuli were presented with Presentation^{TM} software (Neurobehavioral Systems, Inc, California, United States of America) and delivered with a data projector (Panasonic PT-DZ110XEJ). The subjects viewed the stimuli approximately from a 35-cm distance via a mirror. For all subjects, 12 experimental runs with six different measurement protocols were measured: one protocol with standard EPI sequence and five with SMS EPI sequences with different acceleration factors. Both temporally different variations of runs where measured with each protocol. The order of protocols and the temporal variation of multifocal runs were independently randomized for each subjects to avoid similar effects of fatigue across the subjects to affect the results. Subjects were not told which protocols were being performed during which experimental run. The total measurement time with two structural scans was approximately one hour.

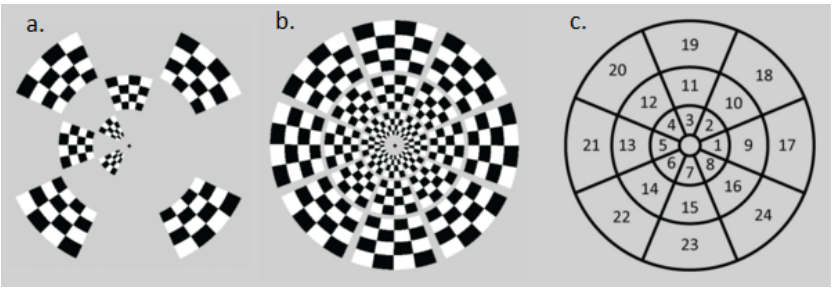

Figure 3.1: Multifocal stimulus. a) One example of the 24-region multifocal stimulus. b) Visual field is divided in to 24 regions and c) each region have its own number. The image is adapted from Ref. [53].

3.2 Subjects

Ten healthy volunteers (7 female, 3 male) were recruited for this study. The vision of the subjects was normal or corrected to normal. Their ages varied between 18 and 47 years, with standard deviation of 8.3 and averaged age 22.5. The subjects are coded to be S2–S11.

The subjects signed an informed consent and a safety questionnaire at their arrival to the laboratory. In addition, an experimental design was roughly presented and the passive viewing task instructed to the subject. All experimental procedures were approved by Aalto University Research Ethic Committee.

3.3 Data acquisition

All fMRI data were acquired at the AMI Centre (Aalto NeuroImaging, Aalto University, Espoo, Finland) with a 3 Tesla MAGNETOM Skyra MRI scanner (Siemens Healthcare, Erlangen, Germany).

3.3.1 Phantom measurements

Prior to the human experiments, I did several MRI phantom measurements with both 30 and 32 channel head coil arrays to calculate basic SNR characteristics for all protocols. Phantom is a specially designed object that is imaged in magnetic field. In this work, I used Siemens MRI phantom which size was 5300 ml and which contained the solution of nickel sulfate, water and sodium chloride.

Phantom measurements were done with the same protocols than the human measurements. The total time of one scanning run of phantom was between 1 and 1.5 minutes. In addition, since partial Fourier parameter was used in the human experiments, I compared what effects it has to SNR with SMS EPI sequences. For this phantom measurements with modified protocols using partial Fourier 7/8, 6/8 and without using the partial Fourier parameter were done. The protocols were modified so that the TR in the standard protocol was 1920 ms and used TE was increased to be 37 ms for all protocols.

3.3.2 Human measurements

The performance of the subject was monitored with EyeLink 1000 plus eye tracking system. This enabled the observation of whether the subject's eye

focus stayed at the fixation dot or not. The visual field shifts with eye position [44] and therefore the monitoring increases the reliability of results. Any data of subjects were not dismissed based on the data of eye tracker.

Most of the subjects were measured with a 32 channel head coil array. Because of the challenge to calibrate the eye tracker, two subjects were measured with a 30 channel head coil array (S5 and S8). Structural images of subjects were acquired with the T_1 Magnetization Prepared Rapid Gradient Echo (MRRAGE) sequence with following parameters: TR = 2530 ms, TE = 3.3 ms, field of view (FOV) = 256 mm, slice thickness = 1.0 mm, phase encoding direction from anterior to posterior, voxel size $1.0 \times 1.0 \times 1.0$ mm^3 and slices per slab 176.

The functional data were acquired using six different T_2^*-weighted imaging protocols: a standard EPI protocol and five SMS EPI protocols with different acceleration factors. In SMS EPI sequences, the number of slices is divided with the used slice acceleration factor. In this experiment, in order to compare different protocols, the number of slices had to be same in all sequences. Therefore, I decided to acquire 24 slices and use simultaneous multi-slice (SMS) acceleration factors 2, 4, 8 and SMS acceleration factor 2 with GRAPPA reduction 2 and SMS acceleration factor 4 with GRAPPA reduction 2. Thus, I was able to compare both small SMS acceleration factors that have showed good results in previous studies [4, 9, 10, 41, 54] and also clearly bigger ones as a contrast. In addition, these acceleration factors enable the comparison of the effects of GRAPPA accelerations to SMS EPI sequences in my experimental design. Hereafter the functional protocols are referred to be as *stand*, *sms2*, *sms4*, *sms8*, *sms2 GRAPPA2* and *sms4 GRAPPA2* (see Table 3.1).

For all functional imaging protocols, the following common parameters were used: TE = 30 ms, slices = 24, FOV = 200 mm, phase partial Fourier 7/8, base resolution 80, bandwith 2084 Hz/pixel, phase encoding direction from feet to head, voxel size $2.5 \times 2.5 \times 2.5$ mm^3 and matrix 64×64. With these parameters the used phase partial Fourier 7/8 parameter was required to have the same TE value for all functional protocols. TE affects the BOLD signal [55, 56] when varying TE values would have affected negatively the comparison between protocols. The optimal TE value for fMRI at 3 T ranges between 30 to 40 ms [42].

For each SMS EPI protocol, TR was set to be the smallest possible multiple of 7200 ms that was the duration of one miniblock of visual stimulation. In standard EPI protocol, TR was set to be the same 1800 ms as in Henriksson and colleagues [11]. In other protocols, TR was reduced to be 900, 720, 400, 360 and 240 ms. For five subjects (S2–S6) the flip angle was 60° in every functional imaging protocols and for the other five subjects the flip

angle was optimised to be the Ernst angle based on the respective TR values and an approximate gray matter T_1 value of 1470 ms [14] at 3 T. The imaging parameters that were different between the protocols are summarized in Table 3.1.

Parameters of functional data acquisition protocols					
Protocol	TR (ms)	Volumes	Flip angle (degree) **S2–S6**	Flip angle (degree) **S7–S11**	Echo spacing (ms)
stand	1800	136	60	73	0.72
sms2	900	268	60	57	0.57
sms4	400	598	60	41	0.60
sms8	240	994	60	32	0.60
sms2 GRAPPA2	720	334	60	53	0.64
sms4 GRAPPA2	360	664	60	39	0.64

Table 3.1: Imaging parameters that differ between the protocols.

3.4 Data analysis

3.4.1 Signal-to-noise ratio

Signal-to-noise ratio (SNR) is one way to measure the scanner stability for fMRI. In this work, one aim was to find out how SNR value changes related to the used acceleration factor of SMS EPI sequences. SNR values were calculated from different protocols of phantom and the human measurements. All SNR calculations were based on Weiskoff [57]:

$$\mathrm{SNR} = \frac{\sum_i m_i}{1.53 \sum_i s_i}, \tag{3.1}$$

where m_i is the mean of signals of the interested region and s_i is the standard deviation of the background. In SNR calculations, it is important to do calculations from such time points where the steady state image is already reached. Therefore, I calculated all SNR values (related to both phantom and human measurements) from the slices of the middle time point of each experimental run.

From phantom measurements, SNR values were calculated from five different locations: in the middle of phantom, top part of the phantom, lowest

part of the phantom, right and left side of the phantom. Figure 3.2 illustrates these locations on a slice. The mean signal values of these locations were calculated from square areas of every slice from same locations of all slices. The standard deviation of background noise was calculated from four different locations of every slice. These locations were same for all slices and far away from both the phantom and any image artifact associated with it. With phantom measurements I compared how SNR changes between different SMS EPI protocols and what effects the partial Fourier parameter has to SNR.

From human data, local SNR values were calculated the same way than the SNR calculations with the phantom. The mean signal was calculated as an arithmetic mean of all slices from the whole brain region by using a brain mask. The standard deviation of background noise was calculated as an arithmetic mean from four different locations of every slice. Since two experimental runs were measured with each protocol, the local SNR values were first calculated separately for both runs. The final local SNR value was then the mean of these two calculated values.

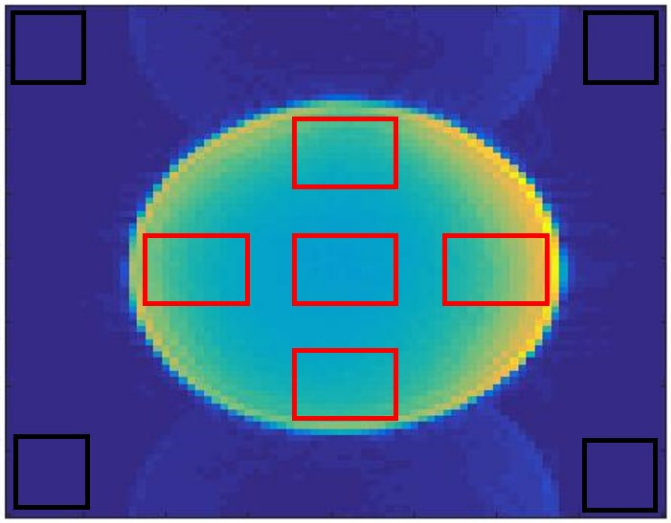

Figure 3.2: In phantom measurements, local SNR values are calculated from five different locations. These locations are illustrated with red squares. The mean signal of these locations are calculated from every slices from the same locations of all slices. The standard deviation of background noise is calculated from four different locations of every slice. These locations are illustrated with black squares and they are far away from the phantom and any image artifact associated with it.

3.4.2 Pre-processing

In the Thesis, pre-processing, statistical analysis and creation of retinotopic maps are all based on the analysis pipeline in Henriksson and colleagues [11]. I used the FreeSurfer software package to segment and reconstruct the borders between white and gray matter from structural images of each subjects. The functional data was analysed with SPM12 (Welcome Department of Imaging Neuroscience, London, UK, [58]) Matlab^{TM} toolbox.

To reduce non-task related variables, I preprocessed the data with SPM12 software following standard pre-processing steps. First, raw functional data were converted to the neuroimaging informatics technology initiative (NIfTI) format. Then acquisition time differences of EPI slices were corrected with temporal interpolation. Because with SMS EPI sequences two or more slices are acquired at the same time, I entered the slice timing for each slice individually in milliseconds. In this case, as the reference slice I used a reference time in millisecond instead of usually used the slice index of the reference slice. For data acquired using a Siemens scanner, slice acquisition times can be acquired directly from the dicom header. Also the head motion during measurements was corrected because head movements create artifacts to the analysis of functional series [59]. Motion correction was done with a rigid-body transformation with SPM12 software. The data were not normalized to the standard coordinate but all the data were analysed in subjects' own coordinates to preserve spatial resolution. For the same reason I did not apply any spatial smoothing.

3.4.3 Statistical analyses

Statistical parametric maps test hypotheses about regionally specific effects in the data. Most of them are based on linear models such as t-tests and correlation coefficients which is a special case of the general linear model (GLM). In this statistical framework, each voxel is analysed separately using a test statistic [60]. The data were analysed by mean of statistical parametric mapping as implemented in SPM12 software.

General linear model

GLM models the time series in each voxel as a linear combination of model functions and random noise. With matrix notations it is expressed as

$$\mathbf{Y} = \mathbf{X}\beta + \epsilon, \tag{3.2}$$

where $\mathbf{Y}$ is a vector that contains the measured fMRI BOLD signal at a given voxel, $\mathbf{X}$ represents the design matrix which columns contain the expected

responses, β is a parameter vector that contains unknown weighting factors for the columns of the design matrix and ϵ is an error matrix. The optimal estimations of β weights

$$\beta = (\mathbf{X}^T\mathbf{X})^{-1}\mathbf{X}^T\mathbf{Y} \tag{3.3}$$

that best describe the data are obtained when the sum of squared errors

$$\sum_{i=1}^{N} \epsilon_i^2, \tag{3.4}$$

where N is the number of time points, is minimized. In GLM there is the assumption that error terms are identically and normally distributed, $\epsilon(t) = \mathbf{N}(0, \sigma^2 I)$ [60].

The design matrix $\mathbf{X}$ defines the experimental design. Each row of the design matrix corresponds one time point of the measured data and each column is constructed to reflect a specific factor (known as regressor) that is thought to influence the outcome of experiment. Typically, there are also additional columns for non-task related variables such as low-frequency drifts if they are not removed during prepossessing. In this experiment, the timing of the stimulus blocks were entered as regressors of interest and parameters of head motion were included to the design matrix as nuisance variables.

Hemodynamic response function (HRF) convolution

The statistical models are improved by convolving the temporal pattern of the stimulation with the canonical hemodynamic response model. If $\mathbf{S}$ is a convolution matrix which rows represent the HRF, a generalized linear model is:

$$\mathbf{SY} = \mathbf{SX}\beta + \mathbf{Se}. \tag{3.5}$$

A typical filter operation related to HRF convolution is high-pass filtering. It removes the noise of physical and physiological sources such as scanner drift and respiratory frequency components. However, noise components which are in the same frequency level than the effects of interest and correlate with the hemodynamics can not be eliminated with the high-pass filter [61]. This kind of noise can induce temporal correlation in residual error term ϵ, when the assumption that error terms are identically and independently distributed does not hold [61]. In this Thesis, I improved the statistical models using HRF convolution.

Estimation of temporal correlations

Modelling and removing temporal correlations is essential to avoid overestimation of functional sensitivity and increased false-positive rates. In conventional fMRI studies, temporal correlations are characterized in terms of a first order autoregressive (AR(1)) model and then removed via prewhitening [62, 63]. Although AR(1) model estimates well the temporal correlations of standard EPI sequences, previous studies [40, 63, 64] show that more elaborate models are needed for rapidly sampled data. Increase in sampling rate causes increase in temporal correlations [65]. Hence, using AR(1) model for accelerated sequences, might result in increased false positives [63]. Because in this work I evaluated SMS EPI sequences and part of the data was acquired with a very short TR, I decided not to use a conventional AR(1) model but a more complex model implemented in SPM12 software under the name "FAST" [66].

Conventionally used AR(1) model uses only two components to model temporal correlations, but AR(FAST) option uses a dictionary of exponential covariance components to model temporal correlations. According to Corbin and colleagues, the implemented AR(FAST) option in SPM12 is more powerful when TR is 1400 ms or smaller [66]. Since the effects of TR to t-max value is related to AR modelling [54], I decided to use AR(FAST) option to model all the data even though TR in the standard protocol was 1800 ms.

Statistical testing

The most common method to make inferences about activation related to a task is based on classical statistics. The significance of the estimated weighting factors of β was tested with t-statistics. The t-value is

$$t = \frac{c^T \beta_i}{\sqrt{Var(c^T \beta_i)}}, \tag{3.6}$$

where c is a contrast vector. Together the t-values of all voxels form a whole statistical parametric map, SPM(t)-map [60].

In functional imaging there are many statistic values and without prior information of where in the brain the effect will occur the hypothesis refers to the whole volume of statistics. Therefore, one has to determine if the huge volume shows any evidence of the effect of interest. Because the question is now about the volume or 'family' of voxel statistics, the possible risk is the family-wise error (FWE) rate. The FWE is the probability that a family of voxel values could have risen by chance and its null hypothesis is that the activation is zero everywhere. The FWE null hypothesis is tested with

applying a critical height threshold (t-value) separately to all of the statistical values [61].

The multiple comparison problem of functional imaging is conventionally solved by Bonferroni correction which is a simple FWE rate thresholding method [61]. However, the Bonferroni correction is too conservative in most cases and thus a random field theory (RFT) can be used to correct the probability values (p-values) [61]. In this study I used a particular threshold value 0.05 ($p_{FWE} = 0.05$), which is typical in fMRI studies, to analyse all of the protocols.

3.4.4 Value, location and cluster size of maximum t-scores

With multifocal fMRI method, 24 multifocal regions were mapped with six different protocols. Between the protocols I compared the observed activation clusters of each region. Are there differences between the achieved maximum t-score values of activation clusters of the protocols, are the maximum t-scores achieved from the same locations with all the protocols and are there differences between the sizes of the activation clusters depending on the used protocol. The factors were examined by picking out the values of the properties from each multifocal region of each protocol separately. The values of each region were then compared to the values of the same particular regions of each different protocol. This kind of comparing is a simple way to roughly evaluate and compare different SMS EPI protocols.

In the Thesis, I analysed the data of subjects individually and kept the data with optimal flip angles separated from the data with unoptimised flip angles. Hereafter a maximum t-score is generally referred to be t-max.

The larger the t-value is the less likely it is that the observed activation is the result of noise fluctuations [67]. Since there were 24 regions and 6 different protocols, I did an average comparison of t-max values to better perceive the big picture. In the average comparison, an arithmetic mean of t-max values over all regions was calculated separately for each protocol. The gotten arithmetic means of protocols were then compared to each other. The arithmetic mean of one protocol was calculated as follow:

$$AM_{t_{max}} = \frac{1}{n}\sum_{i=1}^{n} t_i, \tag{3.7}$$

where n is the total number of regions (24 in this work), i denotes the region and t_i is the value of t-max in region i.

The location of t-max is the location from where the maximal t-score of activation is achieved. There is evidence that with an acceleration factor 4 or more a rate of a false-positive activation increases [9]. Because of this I compared how well the location of the t-max of each region stayed in the same place with different acceleration factors. Even though, the t-max might be bigger with higher acceleration factors, it might be measured from a completely different location due to slice leakage artifacts.

The location of t-maxes were compared by calculating the average location of them over all protocols. Then the distances between the calculated average locations and the original locations of t-maxes were calculated separately for each protocol. After this, the arithmetic mean of distances were calculated over all regions separately for each protocol. The achieved average distance of each protocol was then finally compared to each other.

I also compared cluster sizes related to t-max. The size of clusters might have effect to the final multifocal maps since small clusters cause less continuous maps. The size of clusters related t-max were compared by calculating the arithmetic mean of cluster sizes over all regions of each protocol separately. Then the achieved results were compared to each other. To redeem more information from cluster size analysis, multifocal regions were also divided to three groups: multifocal regions 1–8, 9–16 and 17–24. The division was made from the model of multifocal stimulus (inner, middle and outer circles).

3.4.5 Retinotopic maps

The data of each protocol were constructed separately to polar angle and eccentricity maps using weighted averaging of the responses. To estimate the preferred visual filed location at each voxel, the t-values of the multifocal regions at each voxel calculated in statistical analyses process and the locations of these regions expressed as a number in the complex plane were needed. The used method to construct retinotopic maps is similar used by Hansen and colleagues [68] and later also used in the reference article Henriksson and colleagues [11].

Because the polar angle is a circular quantity, I constructed the polar angles maps using weighter vector averaging of the responses:

$$\theta_w = \arctan(2(b, a)), \tag{3.8}$$

where a is

$$a = \frac{\sum_{i=1}^{N} |R_i|^+ \cos(\theta_i)}{\sum_{i=1}^{N} |R_i|^+} \tag{3.9}$$

and b is

$$b = \frac{\sum_{i=1}^{N} |R_i|^+ \sin(\theta_i)}{\sum_{i=1}^{N} |R_i|^+}. \tag{3.10}$$

In equations, N is the number of stimulus regions i.e. 24 in this work, R_i is the fMRI signal change and θ_i is the polar angle of the different stimuli (i). All voxels whose t-values where less than 3 were omitted from maps to reduce noise.

The eccentricity maps were constructed very similar way than polar angle maps by calculating a weighted eccentricity value e_w for each voxel:

$$e_w = \frac{\sum_{i=1}^{N} |R_i|^+ e_w}{\sum_{i=1}^{N} |R_i|^+}, \tag{3.11}$$

where other variables are same than in polar map calculations but e_w are eccentricities of different stimuli (i). Also in construction of eccentricity maps all voxels with t-values less than 3 were omitted. Once the maps were reconstructed they were visualised with FreeSurfer software.

Chapter 4

Results

This chapter presents the results from my analysis with different visualisations including both phantom and human measurements. Data with optimised flip angles are kept apart from the data measured with unoptimised flip angels.

4.1 Signal-to-noise ratio

4.1.1 Phantom measurements

Before the human experiments, SMS EPI protocols were characterized with phantom measurements. One scan of all six protocols were measured using both 32 and 30 head coil arrays. The used flip angles were 60° in every protocol. The local SNR values were calculated from five different locations: in the middle, top, bottom, right and left part of the phantom. The SNR characteristics of all the protocols are illustrated in Figure 4.1. The bar graphs show the local SNR values of different locations of the phantom with different colors.

Regardless of the used head coil, the results are quite similar: SNR value decreases significantly with slice acceleration factors 8 and 4 when GRAPPA acceleration 2 is added. The slice acceleration factor 2 (*sms2*) results in the highest local SNR values. This result indicates that there might be a possibility that the *sms2* protocol have improving effects to multifocal fMRI.

In addition, I investigated what effect the partial Fourier parameter has to SNR with SMS EPI protocols. I compared the situations were the partial Fourier was not used, it was set to be 6/8 or 7/8. As a results, I found out that using partial Fourier of 7/8 results in slightly smaller local SNR values than using partial Fourier of 6/8. The SNR was the lowest without partial

Fourier parameter. In human measurements, partial Fourier of 7/8 was used to get the same TE value for each protocol.

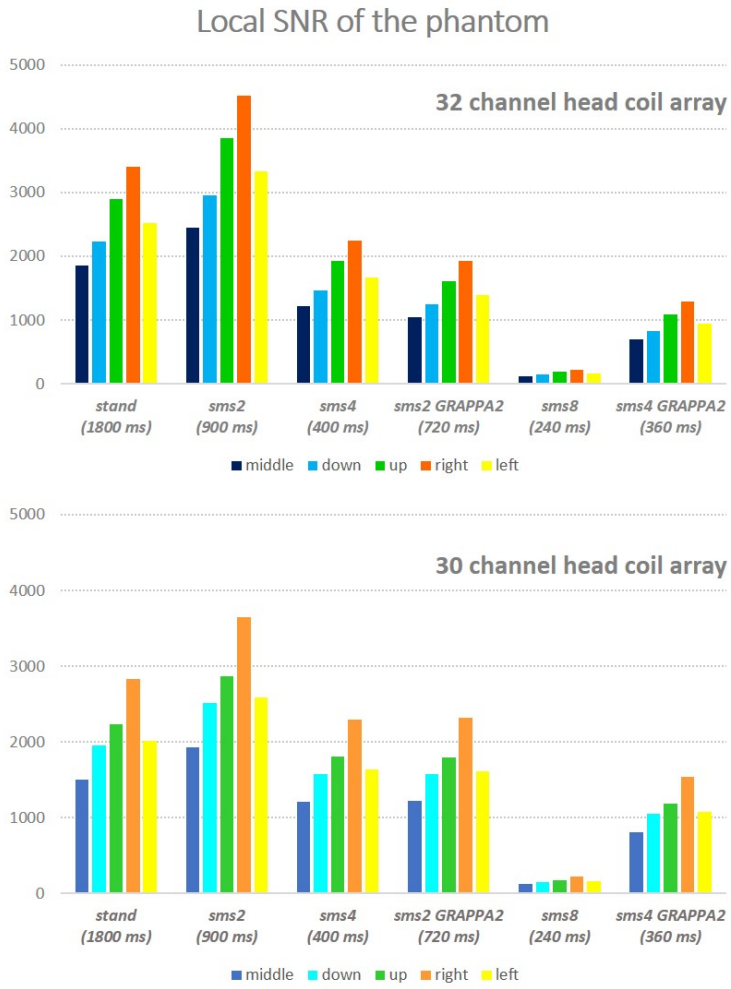

Figure 4.1: Local SNR values of the phantom with 32 (above) and 30 (below) channel head coil arrays. SNR values are calculated from the middle time point of the each experimental run to ensure that the steady state image is already reached. From phantom data, the local SNR values were calculated from five different locations: in the middle, top, bottom, left and right part of the phantom. Mean signal was calculated from these locations over all slices. In the bar graphs these locations are color coded and the protocols are in the x-axis. Regardless of the used head coil arrays the *sms2* produced the highest local SNR values and the *sms8* the lowest.

4.1.2 Human measurements

Local SNR values were also calculated for all the subjects by using brain mask. SNR was calculated from an image from the middle of time series for two reason: To ensure that the magnetization is already reached the steady state and because the middle image should be the closest (on average) to other images in the time series [69]. The results of subjects are illustrated in Figure 4.2. The results of subjects whose data were acquired with optimised flip angles (S7–S11) are kept separately from the results of the subjects whose data were acquired with unoptimised flip angles (S2–S6). Since two experimental runs were scanned with each protocol the reported results are an average of the results of both runs.

Although the results of the local SNR values varied between the subjects, for all the protocols *sms8* and *sms4 GRAPPA2* produced the lowest SNR values. For the most subjects (S2, S4, S6, S7, S9 and S11), SNR was the highest with the *stand* protocol and it decreased as used slice acceleration factors increased and the used TR value decreased. For S3, S8 and S10, SNR was the highest with the *sms2 GRAPPA2* protocol. For these subjects also the protocols *sms2* and *sms4* produced higher local SNR values than the *stand*. Since, the SNR results varied significantly between subjects further research are needed.

In Figure 4.3, two slices of the data of S10 and S11 from the middle image of the time series are illustrated. The presented slices are 2 and 7. Even though there were some variation in local SNR results between the subjects S10 and S11 (See Figure 4.2) the signal intensity decreases similarly between the protocols. The observation indicates that the SNR variation might be the result from differences in standard deviation of noise signal. For both subjects the signal intensity is the highest with the *stand* and it decreases as the TR used decreases. This observation is reasonable since the shortened TR reduces steady state magnetisation that decreases signal intensity. The similar results were seen with all other subjects whose data were acquired with optimised flip angles.

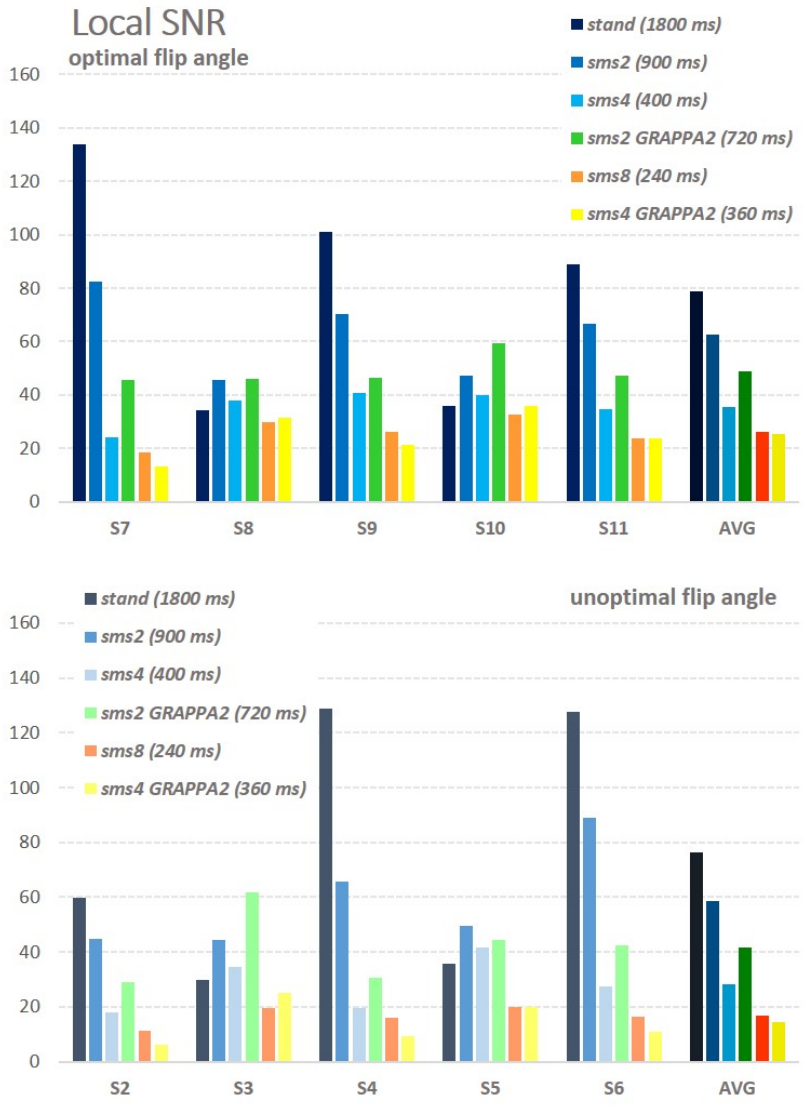

Figure 4.2: Local SNR values of subjects. In human measurements, local SNR values are calculated using brain mask. The data acquired with optimised flip angles are kept separately from the data acquired with unoptimised flip angles. Even though there is variation between subjects the protocols *sms8* and *sms4 GRAPPA2* produced the lowest SNR values for all the subjects. In these protocols the TR used was the shortest (240 and 360 ms). For subjects S2, S4, S6, S7, S9 and S11 the protocol *stand* produced the highest SNR values and it decreased as the TR used decreased. In general, calculated local SNR values are higher if the data is acquired with optimised flip angles. In both bar graphs, averaged SNR results (AVG) are calculated over all subjects in question.

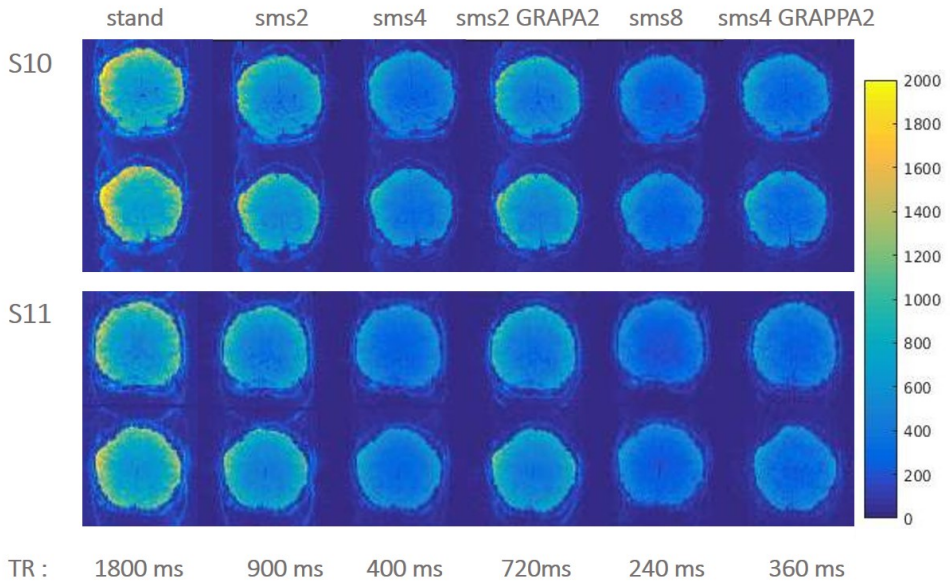

Figure 4.3: Slices 2 and 7 of S10 and S11 from the middle image of the time series are illustrated. The signal intensity is the highest with the *stand* and it reduces as the TR used decreases.

4.2 Visualization of fMRI data

4.2.1 FMRI time series

To roughly compare how the data of different protocols look like, I plotted the fMRI time series of particular voxels of each sequences. The selected voxels were the voxels of t-maxes. For the reliable comparison, the plotted voxels were same for all six protocols. In Figure 4.4, the time series of the t-max voxel of the multifocal region 17 is plotted. The multifocal region 17 is near the horizontal meridian that runs along the calcarine sulcus and thus the activation of it is in V1.

From Figure 4.4 one can see that the higher the used slice acceleration factor is the noisier the data is. Consistent results were achieved from other multifocal regions and with other subjects. Because the SMS data look much noisier than the data of standard EPI protocol, it indicates that the SNR decreases with higher acceleration factors. This is consistent with the presented local SNR results since the *sms8* and the *sms4 GRAPPA2* produced the lowest local SNR values. The red lines in Figure 4.4 are GLM mod-

elling results of each data. From this example one can see that the models look similar regardless of the used protocol which indicates that the model captures the same activation despite the used protocol.

As a comparison in Figure 4.5 only the estimations from the time series of the t-max voxel of region 11 (S10) are plotted. One can see that there is slight variations between protocols. In general, depending on the multifocal region there are differences with that how well the model captures the same activation. With multifocal regions 9–16, that are located into the middle ring of the stimulus, the variation was smallest especially with the regions that were near the horizontal meridian. The activation of multifocal regions near the horizontal meridian are in clearly in V1. The regions in the middle ring are rounded with other regions and thus the activation of these regions are precise. In the multifocal regions, that were near the vertical meridian (e.g the regions 3, 11 and 19) there were slightly more variation in the plotted estimations of the time series. The activation of these regions are on the border of V1 which might explain the possible variation. However, in all regions with all the subjects the model mainly captures the same activation despite the used protocol. The plotted estimations in Figure 4.5 illustrates the example of the clearest variation I was saw in any subject.

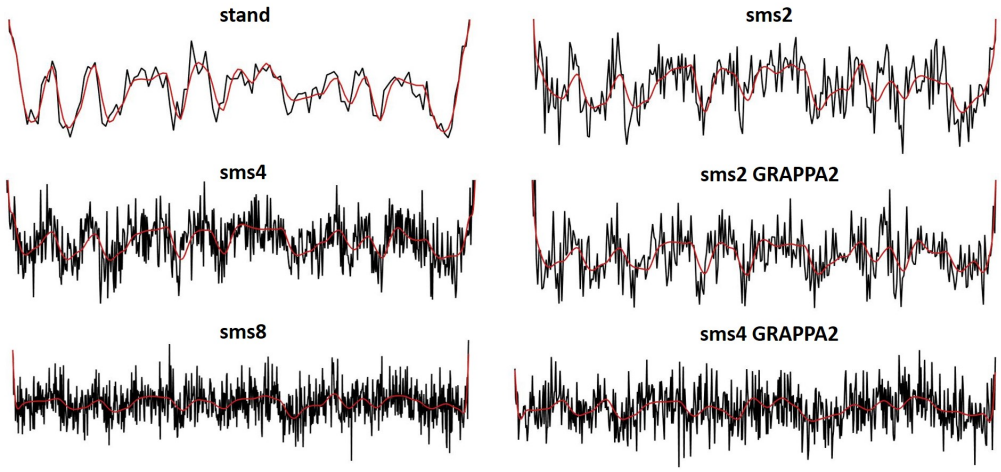

Figure 4.4: FMRI time series of a voxel from multifocal region 17 of S9. The black lines illustrate the data and the red lines are estimated models. The plotted time series are from the voxel where the maximum t-score value is achieved. The plotted voxel was same for all protocols. The results were similar for all subjects and all regions. The data are noisier with higher acceleration factors.

Figure 4.5: GLM modeling results of each protocol. The models are estimations from the time series of t-max voxel of region 11 of S10. One can see that there is slight variations between the protocols. The region 11 is near the vertical meridian and thus its activation cluster is on the border of V1 which might explain the variation. The illustrated example has the clearest variation I was saw in any subject in any region.

4.2.2 Examples of activation result

In Figure 4.6, the activation of the multifocal region 9 of S10 and in Figure 4.7 the activation of the multifocal region 21 of S9 are shown on the structural images. The data of S10 and S9 were acquired with optimised flip angles. In both figures, the first image illustrates from where the closer images are taken (the blue area). The zoomed in images show the cluster of the t-max and therefore the illustrated slices are not the same with all the protocols. The color scales are specified for each protocol.

The activation clusters are correctly localized in the occipital cortex with all imaging protocols. Since multifocal regions 9 and 21 are near the horizontal meridian which is represented along the calcarine sulcus, the illustrated t-max values are in clusters near the calcarine sulcus. Hence the activation of these regions are in V1. The activation look similar with all sequences except the activation of region 21 of the *sms8* of S9. In Figure 4.7, the activation clusters of t-max of region 21 are illustrated in a and the activation b illustrates the achieved activation clusters of the second highest t-score value. With the *sms8* the activation of the second highest t-score value looked similar with the activation achieved with the other sequences. The observation indicates that the t-max of the *sms8* is achieved from the different location compared to the other sequences. Since previous studies have indicated that the high slice acceleration factors increase false positives rate and cause slice leakage artifacts [9, 10], in this work I also examined is the observed activation achieved from the same location with all protocols. I compared the

locations of t-max values and the results are presented in Subsection 4.4.

In general, the observed activation of multifocal regions of all the subjects were similar with the results showed in Figure 4.6 and 4.7. The activation clusters of all regions were on the occipital lobe. And the activation of each region looked mainly similar with all sequences. The differences were only seen with some subjects with higher slice acceleration factors (the protocols *sms8* and *sms4 GRAPPA2*) as in Figure 4.7.

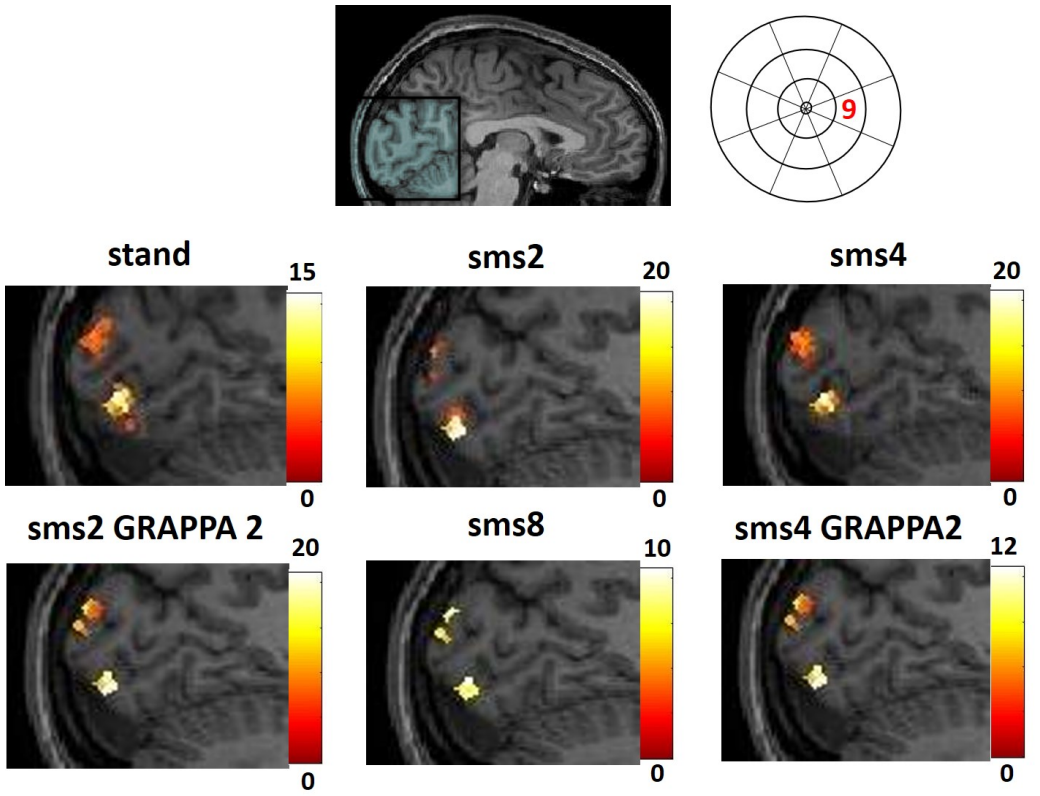

Figure 4.6: The activation of the multifocal region 9 of S10 on the structural image. In the image of the full brain the marked area (blue) illustrates the area from where the closer images are taken. The images of activation show the cluster of the maximum t-score. Hence the illustrated slices are not the same in all images. The color bars are specified to the each sequence. Since the region 9 is near the horizontal meridian that runs along calcarine sulcus the cluster of t-maxes are in V1. With all sequences the activation looks similar and it is on the occipital lobe.

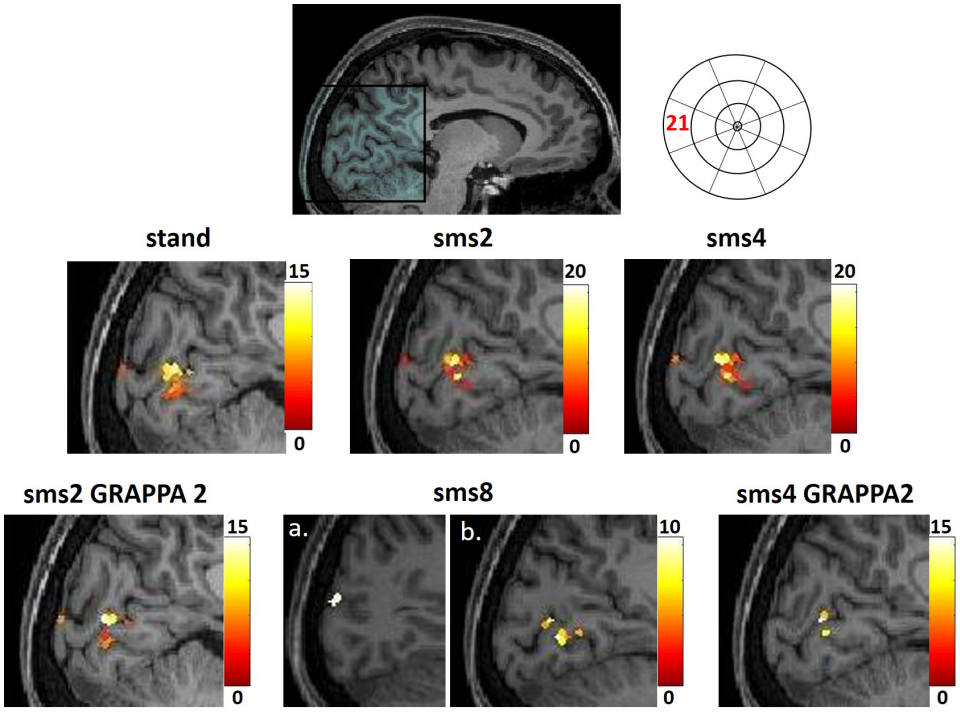

Figure 4.7: The activation of the multifocal region 21 of S9 on the structural image. The structure of the figure is the same compared to Figure 4.6. The multifocal region 21 is near the horizontal meridian which runs along the calcarine sulcus and thus the activation is in V1. In this example, the activation look similar in all sequences except the results of the *sms8*. The activation a illustrates the activation of t-max and b illustrates the activated clusters of the second highest t-score value. The b activation looks similar with the activation achieved with the other sequences. The observation indicates that the location of t-max of *sms8* is different compared to other sequences. One can also see that the activation achieved with the higher slice acceleration factors is smaller.

4.3 T-max values

In this section, I present the maximum t-score values. The larger the t-score values are the less likely it is that observed activation is just the results of noise fluctuations [67]. I have compared the maximum t-score values of each protocol between the regions and also calculated the averaged maximum t-score values over all regions. All the results of maximum t-score values are visualized on bar graphs.

Figure 4.8 shows an overall picture of the results of S7 keeping all 24 multifocal regions separately. Even though there were slight differences between subjects, this figure demonstrates how t-max values differ between different multifocal regions. Different protocols are color coded and the number of multifocal regions are in the x-axis. The data of S7 are acquired with optimised flip angles.

From Figure 4.8 one can see that the lowest t-score values are observed with *sms8* and *sms4 GRAPPA2* protocols. However, these protocols still give significant results in all regions. These were consistent with all subjects whose data were acquired with optimal flip angles. With the data acquired

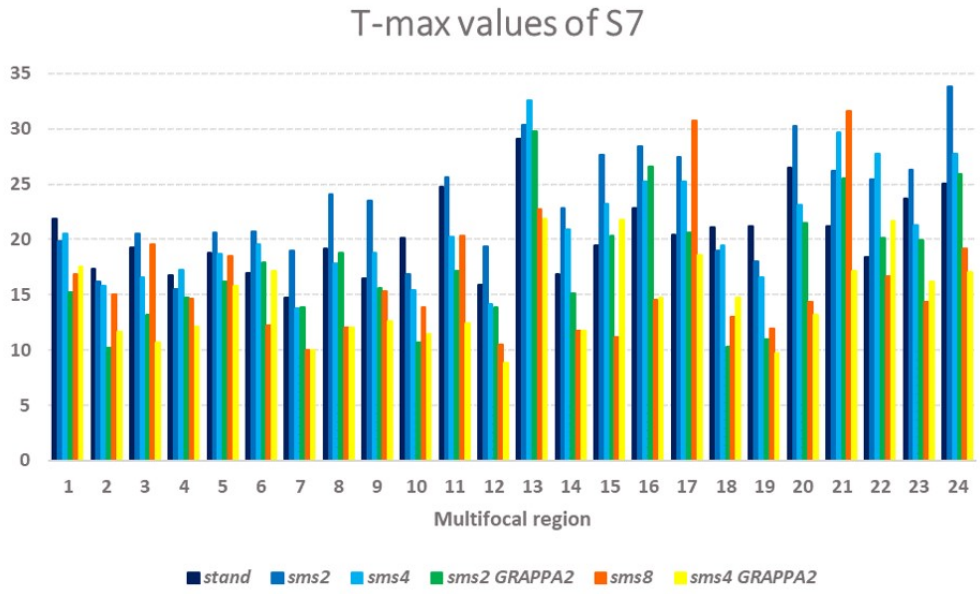

Figure 4.8: Overall picture from t-max values of one subject (S7). The visual field was divided to the 24 multifocal regions. The maximum t-score values from the activated clusters of each region are presented here. The t-max values achieved with different protocols are kept separately and illustrated with different colors. The data presented here were acquired with optimal flip angles. In all the regions even the *sms8* and the *sms4 GRAPPA2* protocols produced significant t-max values even thought the results were lowest compared to the other protocols. The consistent results were seen with all the subjects. However, with the subjects whose data were acquired with unoptimised flip angles the t-max values achieved with the protocols *sms8* and *sms4 GRAPPA2* were significantly lower than the results in this figure.

with unoptimised flip angles the signal intensity is low due to incomplete signal recovery between radio frequency pulses [17] and therefore the higher slice acceleration factors (the protocols *sms8* and *sms4 GRAPPA2*) result in very low t-max values. The effects of low signal intensity was also seen with the results of the *sms4* since the t-max values of the *sms4* were significantly lower when the flip angle was not optimised compared to the values achieved with optimised flip angles.

Figure 4.9 represents the averaged t-max values over all regions of each protocol. Different protocols are color coded. The results of subjects S7–S11 are illustrated in Figure 4.9**a** (data acquired with optimal flip angles) and the results of subjects S2–S6 in Figure 4.9**b** (data acquired with unoptimal flip angles). Figure 4.9 **c** illustrates the averaged results over subjects S7–S11 (black line) and over subjects S2–S6 (red line).

As can be seen in the bar graphs, there is variations between different subjects. For S7 and S10 the protocol *sms2* causes the highest t-score values. While for S3, S8, S9 and S11, the highest t-score values are achieved with the protocol *sms4*. For the others, the highest t-score values are achieved with the *stand*. The *sms8* and the *sms4 GRAPPA2* protocols produce the smallest t-score values except for S8 which smallest t-score values were achieved with the *sms2* protocol.

When observing the line graph (Figure 4.9**c**), where the results of subjects are averaged, one can see that the the highest t-max values with unoptimised flip angles (the red line) is achieved with the *stand* while with the optimised flip angles (the black line) the *sms4* produced the highest t-max values. One can also see that the reduction of t-score values with significantly higher slice acceleration factors is clearer when data is acquired with unoptimised flip angles. This is reasonable result, since with unoptimised flip angles the signal recovery between radio frequency pulses is incomplete, which reduces the signal intensity [17]. The effect is seen clearer with higher slice acceleration factors (the *sms8* and *sms4 GRAPPA2*) since the sampling rate is more accelerated and TR shorter. The same reason explains also that why with the unoptimised flip angles the t-max values of the *sms2* and the *sms4* were lower compared to the values achieved with the *stand* although these two protocols produced higher t-max values than the *stand* with optimised flip angles.

The results achieved with optimised flip angles (S7–S11) were promising to that the moderate slice acceleration factors can be used to improve BOLD sensitivity. Next I will compare the locations of the achieved t-max values. Especially with higher acceleration factors, it is possible that the t-max value is results of noise fluctuation and thus achieved from a complete different location.

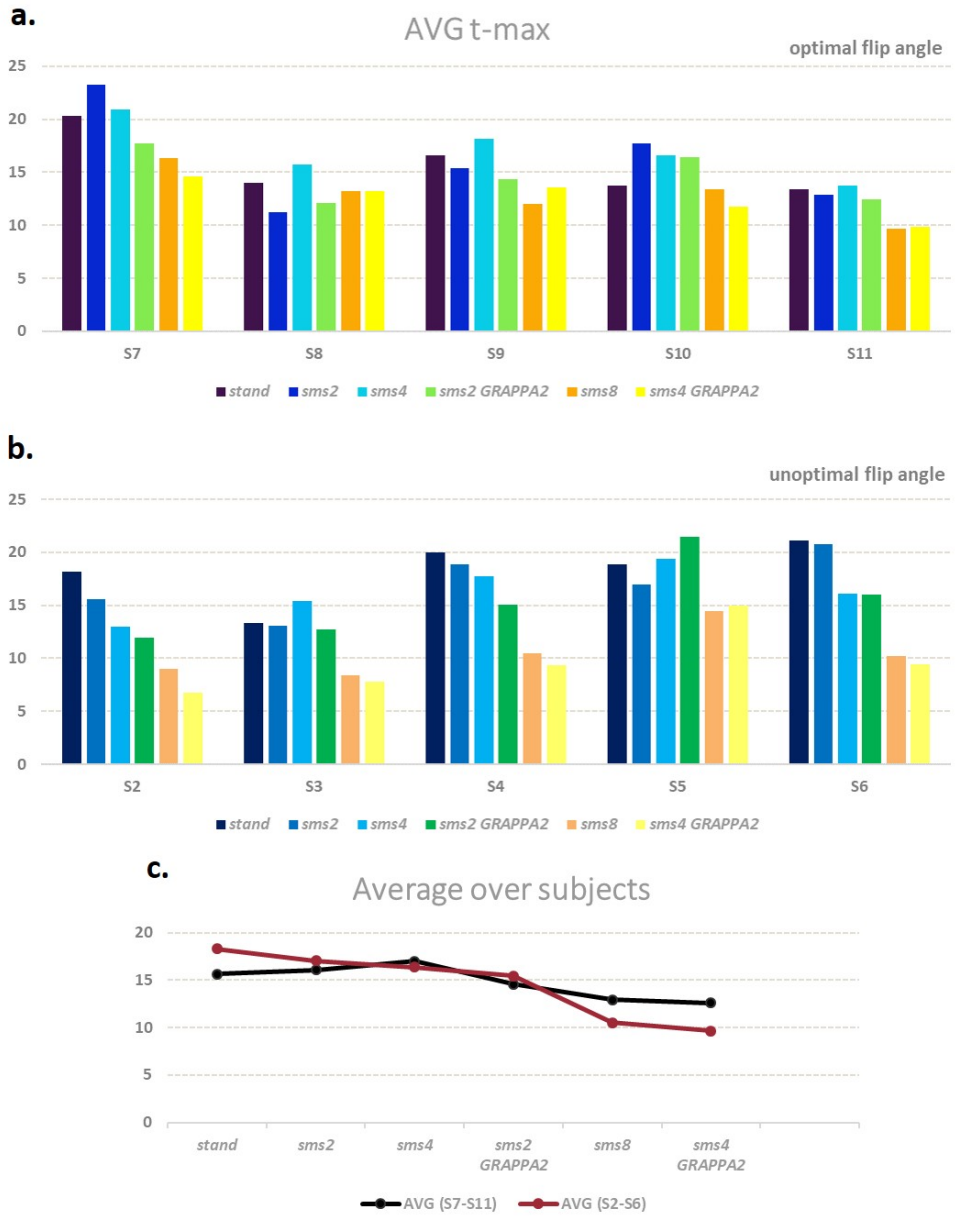

Figure 4.9: Results of averaged t-max values over all regions. In both bar graphs (**a** and **b**), the presented t-max values are achieved by calculating the arithmetic mean of t-max values over all 24 multifocal regions. The averaged t-max values of each protocol are color coded. The subjects are in the x-axis. The results of subjects whose data is acquired with optimised flip angles (S7–S11) are in the bar graph **a** and the results of subject whose data is acquired with unoptimised flip angles are presented in the bar graph **b**. The line graph **c** presents the averaged results over S7–S11 (black line) and S2–S6 (red line).

4.4 Location of t-max values

Since SMS EPI sequences are affected by slice leakage artifacts especially when using high slice acceleration factors, I observed how much the location of achieved maximum t-score values differ between different protocols. If the maximum t-score value of the particular multifocal region is achieved from a completely different location compared to the results of other protocols, there is a large probability that the achieved maximum t-score is results from noise fluctuation. In the other hand, the observation of t-max locations tells if the activation cluster is not in the V1. According to the previous study of Henriksson and colleagues [11] it is known that the t-max values are achieved from the V1 with the single-slice EPI sequence (the *stand).* Thus, the clusters of t-maxes should be located in V1 with all the protocols. With the observation of t-max locations, I ensure that the same clusters are sampled with the each protocol.

Figure 4.10 illustrates the results of how much does the location of t-max values differ between different protocols. The data acquired with optimal flip angles (S7–S11) are presented in the upper graph and the data acquired with unoptimal flip angles (S2–S6) are presented in the lower graph. Both graphs show averaged distances between the original locations of t-max values and their average locations calculated over all protocols. In other words, these results are achieved by calculating first an average location of t-max for each region over all protocols, then calculating the distances between the original locations and calculated average locations and finally calculating an average distance for each protocol over all multifocal regions. The subjects are color coded and the black dashed line illustrates an average results over all subjects in question.

With the *sms8* and the *sms4 GRAPPA2* the calculated distances increase (Figure 4.10). This result indicates that the t-max values are achieved from different locations compared to the other protocols. For further observation, it would be necessary to examine whether the sampled clusters of the *sms8* and the *sms4 GRAPPA2* are still in the V1 or not. If the activated clusters are in completely different locations, they might be the result of slice leakage artifacts. According to Todd and colleagues it is possible that there are false positive activation in slices that are simultaneously acquired due to signal leakage [9]. Between the protocols *stand*, *sms2*, *sms4* and *sms2 GRAPPA2* there are no significant differences in distances. This indicates that between these protocols the t-max values were achieved from the same locations and that the protocols sample the same clusters. The distances are longer with unoptimised flip angles which indicates that the locations of t-max values

vary more between different protocols. One reason for this might again be the reduced signal intensity.

4.5 Cluster sizes

I also compared the size of the clusters of t-max values. In Figure 4.11, the average cluster sizes of each protocol over all regions are presented. The subjects are color coded and the results of S7–S11 (the data acquired with optimised flip angles) are presented in the upper graph and the results of S2–S6 (the data acquired with unoptimised flip angles) in the lower graph. In both graphs, the dark dashed line illustrates the average results over all subjects in question.

There is some variations between different subjects, especially between subjects S2–S6 whose data were acquired with unoptimised flip angles. The observation, indicates again that with optimised flip angles the results are more reliable. Regardless of using optimal or unoptimised flip angles, cluster sizes decrease with higher slice acceleration factors (the protocols *sms8* and *sms4 GRAPPA2*). For most of the subjects the cluster size is the biggest with the *stand* and almost as big with the *sms4*, especially when the data is acquired with optimised flip angles. With the *sms2* protocol the sizes of clusters mainly decrease compared to the *stand* and the *sms4*. The black dashed lines show that with unoptimised flip angles clusters are smaller, especially with higher acceleration factors. The observation is reliable since data acquired with unoptimised flip angles suffer from lower signal intensity [17].

I also compared the cluster sizes by dividing the multifocal regions into three parts: inner, middle and outer rings. The division was made from the multifocal stimulus. Figure 4.12 shows average results of each ring over subjects S7–S11. The clusters are the biggest in regions 1–8 (the inner ring) and the smallest in regions 9–16 (the middle ring). The trend of all three lines is similar.

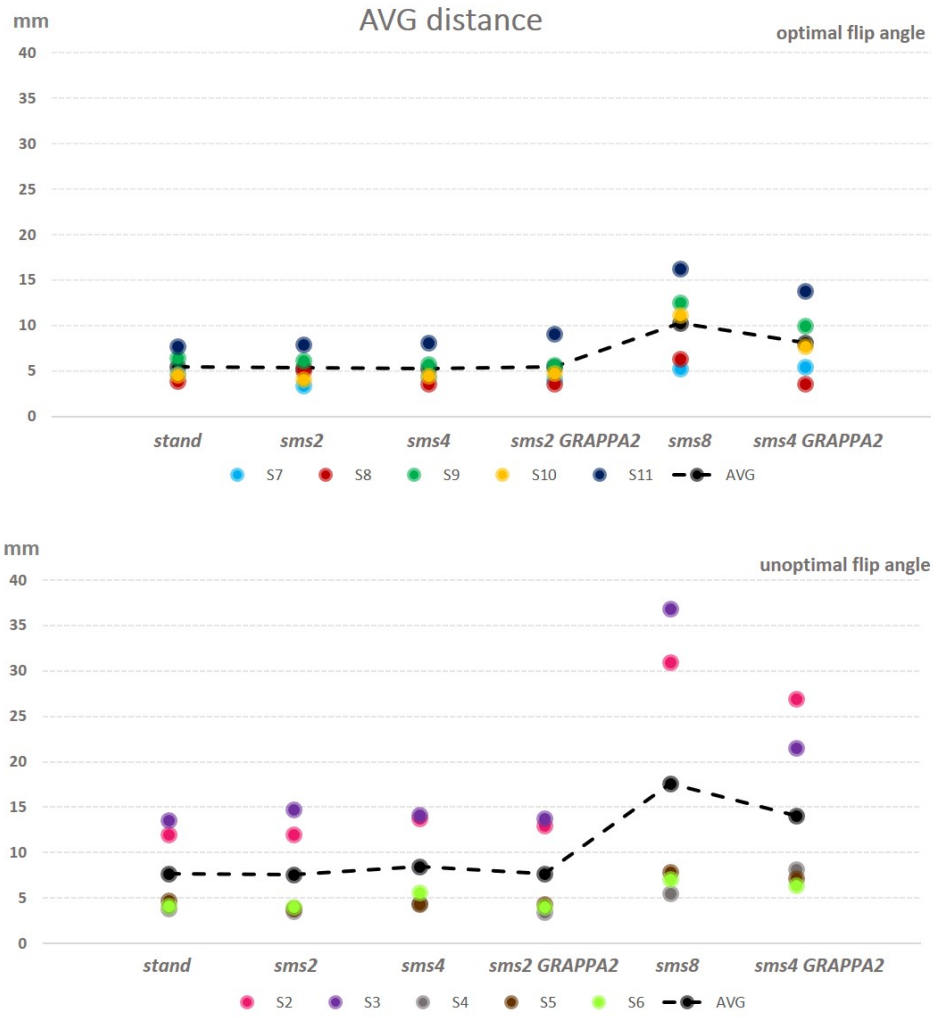

Figure 4.10: The averaged distances of the location of t-maxes over all regions of each protocol. The distance is a gap between the original location of the t-max value and its calculated average location over all protocols. Here the the results are achieved by calculating first the average locations of t-maxes for each region over all protocols. Then the distances between the original locations and the calculated average locations are calculated and finally the average distances for all protocols over all multifocal regions are calculated and these values are presented in both graphs. Subjects are kept separately and they are color coded. Different protocols are in the x-axis. The data of subjects S7–S11 are acquired with optimised flip angles (above) and the data of the subjects S2–S6 are acquired with unoptimised flip angles (below). Both graphs show that with higher slice acceleration factors (the *sms8* and the *sms4 GRAPPA2*) the distance increases which indicates that the locations of t-maxes are different compared to the other protocols. The distances are longer with unoptimised flip angles (below) which indicates that the locations of t-maxes vary more if the used flip angles are not optimised.

Figure 4.11: Averaged sizes of clusters over all regions. Here the sizes of the clusters from where the t-max values are achieved are compared. The presented averaged sizes are calculated over all regions of each protocol. The results of the subjects S7–S11 (data acquired with optimal flip angles) are presented in the upper line graph and the results of the subjects S2–S6 (data acquired with unoptimal flip angles) are presented in the lower line graph. All the subjects are color coded. The protocols are in the x-axis. The dashed black lines illustrate the average results over the subjects in question. There is some variation between subjects, but as an average, one can see that with the higher the used slice acceleration factor is the smaller the cluster sizes are. With optimised flip angles the *sms4* protocol produces almost as large clusters than the *stand* while the *sms2* produces smaller cluster sizes than both of them.

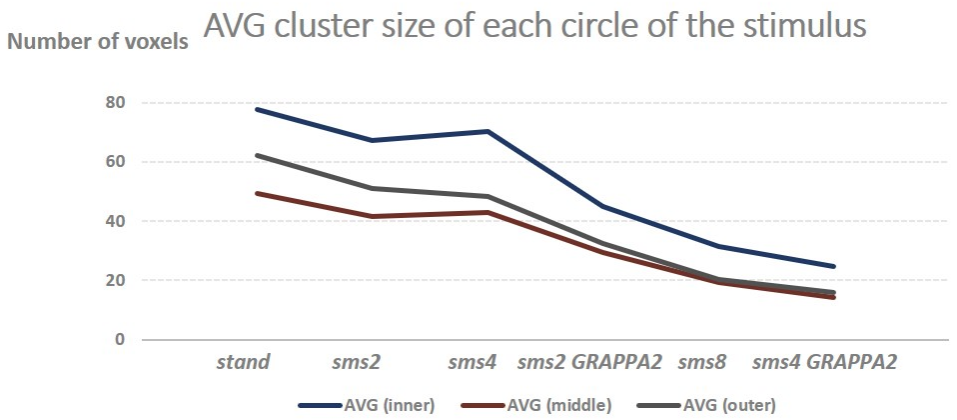

Figure 4.12: Average size of clusters of S7–S11. Multifocal regions are divided to three groups (inner, middle and outer circles of the multifocal stimulus). Regions 1–8 belong to the inner circle, regions 9–16 to the middle circle and the rest regions (17–24) to the outer circle.

4.6 Multifocal maps of visual cortex

Multifocal maps of visual cortex show the borders of visual field areas and they are usually routinely created as a part of visual fMRI studies. In this Thesis, SMS EPI protocols were also evaluated by comparing the retinotopic maps obtained with different SMS acceleration factors. If the multifocal maps of SMS data are good enough, the acquisition time of routinely used multifocal mapping can be reduced. In Figures 4.13 and 4.14, there are multifocal maps (polar angle and eccentricity) of S7 and S9. These multifocal maps are acquired with protocols of optimised flip angles.

One can see that the *stand* protocol produces the smoothest maps. However, multifocal maps acquired with the *sms2* protocol, where the TR used is 900 ms, are also quite smooth. Depending on the subject, also the *sms4* shows quite good outcomes. TR of the *sms4* is 400 ms. With higher acceleration factors (the *sms8* and the *sms4 GRAPPA2*), the multifocal maps are not so continuous than with the *stand*. In the *sms8* the TR is shortened to be 240 ms and in the *sms4 GRAPPA2* it is 360 ms. In general, smoother multifocal maps are acquired with optimised flip angles. However, with all the subjects even the multifocal maps of the *sms8*, clearly shows which part of the brain are related to which visual field areas.

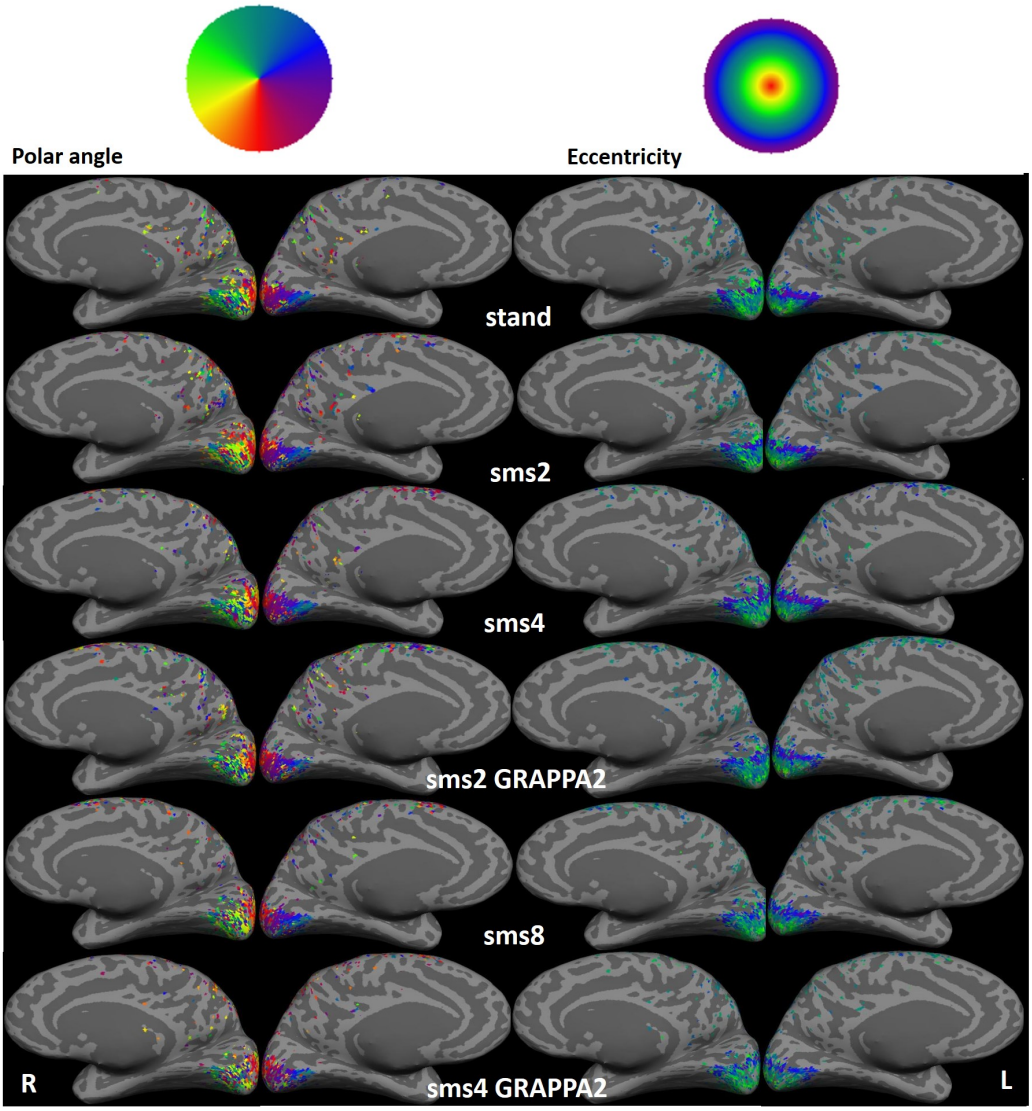

Figure 4.13: Polar angle (left) and eccentricity (right) maps of S7. Data are acquired with optimal flip angles. Achieved multifocal maps are presented on inflated surfaces. The inflated surfaces are reconstructed from 3-D structural volumes with FreeSurfer software [70]. In inflated surfaces, dark gray color illustrates sulcus and light gray color illustrates gyrus. The activation in midsagittal plane of both hemisphere is shown. All protocols produce reasonable multifocal maps. Even with the *sms8* protocol, where the TR is reduced to be 240 ms, one can see which parts of the brain are related to which visual field ares. However, multifocal maps achieved with moderate TR values including TR of 1800, 900 and 400 ms (the protocols *stand*, *sms2* and *sms4*) are smoother compared to the maps achieved with shorter TRs.

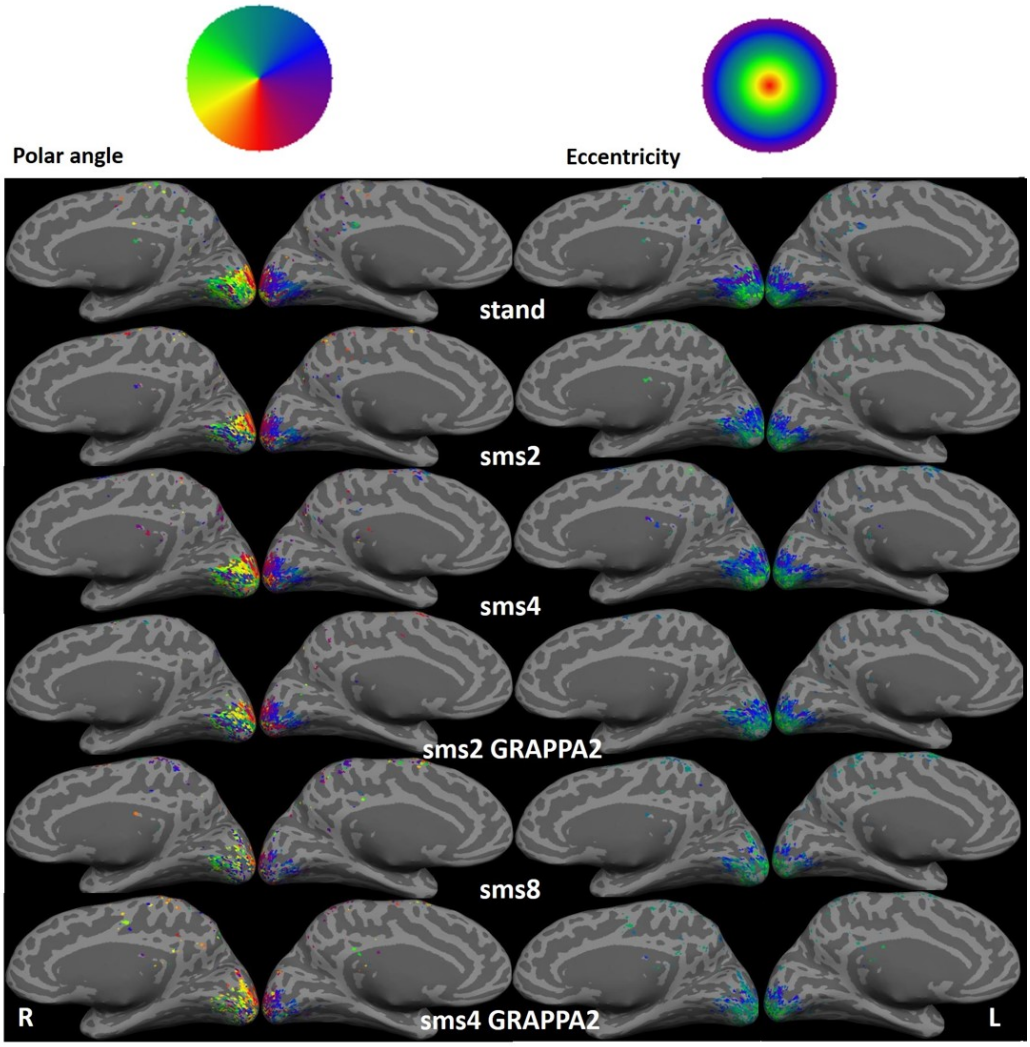

Figure 4.14: Polar angle (left) and eccentricity (right) maps of S9. Data are acquired with optimal flip angles. The calculated maps are presented on inflated surfaces as in Figure 4.13. Sulcus of the brain are illustrated with dark gray color and gyrus of the brain are illustrated with light gray color. The midsagittal plane of both hemispheres are shown. The achieved maps indicates that all protocols produce significant multifocal maps. Multifocal maps acquired with the *stand* (TR is 1800 ms) are the smoothest. With significantly shorter TRs such as 240 and 360 ms (the protocols *sms8* and *sms4 GRAPPA2)* multifocal maps are clearly less smooth. One explanation for this result might be that with shorter TRs the cluster sizes decrease (see Subsection 4.5). The multifocal maps achieved with the protocols *sms2* and *sms4* are also quite smooth but the polar angle maps of them are slightly noisier compared to the maps achieved with the *stand*. In general, SMS EPI protocols produce better outcomes for eccentricity maps.

Chapter 5

Discussion

5.1 Signal-to-noise ratio

SNR results from both phantom and human measurements indicate that significantly higher slice acceleration factors and shorter repetition times decrease SNR. These results are consistent with the results of the previous studies [3, 42, 43]. In this work, the SNR reduction was biggest with the protocol *sms8* where the TR used was reduced to 240 ms. However, especially with phantom measurements, the protocol *sms2* produced higher SNR values than the *stand*. This result is promising for further studies. The TR used in the *sms2* was 900 ms. With phantom measurements, local SNR values of the right side of the phantom were significantly higher than the local SNR values of the left side of the phantom. This observation was unexpected since the SNR value should not vary significantly between the right and the left side of the phantom. Hence, further research of the head coil arrays used and the phantom is needed.

The SNR reduction is due to both the increase in g-factor noise penalty and the decrease in the level of steady state longitudinal magnetization present while imaging at shorter TR [3]. With higher slice acceleration factors, g-factor penalty increases since the slice-aliased data are more difficult to reconstruct. The more slices are acquired simultaneously, the smaller the distance between the simultaneously acquired slices is. This makes it more difficult to separate them from each other even with the blipped CAIPIRINHA technique. The g-factor noise amplification depends on the SMS sequence parameters including slice position, SMS acceleration, in-plane acceleration and shift of blipped CAIPIRINHA [43]. In addition, the geometry of the receiver coil array and the brain affect g-factor noise [43]. Therefore, the amount of g-factor noise is subject specific and spatially non-uniform. These

factors explain why there were large variations between the subjects. The experiments were measured with both 32 and 30 channel head coil arrays. The coil elements of these head coil arrays are located similarly. Because the sensitivity profiles of the coils are similar around the visual cortex, all of the SNR results were comparable with each other.

T_1 relaxation effects will depend on T_1 time of the brain tissue and the additional radio frequency field B_1 [1]. With shorter repetition times, there is less time for signal recovery which leads to lower SNR values [3]. The effect is especially noticeable when the data acquired with unoptimised flip angles are compared to the data acquired with optimised flip angles. With constant 60° flip angles, the SNR reduction of the protocols *sms8* (TR = 240 ms), *sms4 GRAPPA2* (TR = 360 ms) and even *sms4* (TR = 400 ms) were bigger compared to the data acquired with optimised flip angles. With shorter TRs the signal recovery does not complete between radio frequency pulses if the used flip angle is too big and not optimised. Therefore, if the used TR is shortened, it is important to remember to change and optimise the used flip angle with Ernst angle.

According to Setsompop and colleagues, if TR is smaller than T_1 of the tissue, the reduction of SNR due T_1 saturation increases [3]. In this work, the repetition times used were as short as possible with imaging parameters used when only the TR of the *stand* protocol was bigger than T_1 of gray matter (T_1 = 1470 ms [14]). Hence, the evaluated SMS EPI protocols might result higher SNR values if the TR used is more moderately reduced. Trade-offs between benefits of accelerated sampling rates and reduction in SNR are needed. It would be reasonable to study, what kind of SNR results different slice acceleration factors produce with more moderated TR values in multifocal fMRI.

5.2 The optimisation of flip angle

Overall, the results of unoptimised flip angles were worse compared to the results of optimised flip angles. The difference was seen especially with the protocols of higher slice acceleration factors as the *sms8* and the *sms4 GRAPPA2*. The use of unoptimised flip angles produced lower t-score values, smaller cluster sizes, discontinuous and noisier multifocal maps and bigger SNR reductions. In addition, the locations where the maximum t-score values were achieved varied more between the protocols when flip angles were not optimised.

The main reason for these is lower signal intensity due to too slow signal recovery between radio frequency pulses. This is mainly a result from using

too big flip angles compared to the accelerated sampling rate. According to Ernst and colleagues, an optimal flip angle depends on the TR used and T_1 of the tissue [17]. If the TR is radically reduced and the flip angle is not changed, there is not enough time for relaxation which saturates the longitudinal magnetization [3]. This has a direct relation to the SNR reduction as discussed in Subsection 5.1. Lower signal intensity has also a negative impact on other properties since there is less signal that exceeds the threshold value of t-statistics. In general, the results of this work indicate that unoptimised flip angles produce worse outcomes and the negative effects are clearer with higher slice acceleration factors and shorter TRs.

5.3 Characterization of SMS EPI protocols

Given the negative aspects of unoptimised flip angles, in this section I will focus the discussion SMS EPI protocols used with optimised flip angles. According to previous studies [3, 4, 9, 10, 42, 43], with higher slice acceleration factors the g-factor penalty increases, there is more slice leakage artifacts and SNR decreases. The results of this work were consistent with these studies. The protocols *sms8* and *sms4 GRAPPA2* produced the lowest SNR values, smallest t-score values and less smooth multifocal maps. In theory, the use of slice acceleration factor increases echo time, since radio frequency pulses are slightly slower, which reduces the signal [71]. To make it possible to use the same echo time (TE = 30 ms) in all protocols, the partial Fourier 7/8 was used. With partial Fourier, TE can be shortened, but at the same time the used partial Fourier will also reduce the signal [1]. Hence, in the used protocols these effects compensated each other. As already discussed in Subsection 5.1 a short TR and increased g-factor penalty, due to difficulties to reconstruct closely aliased simultaneously acquired slices (slice leakage artifacts), also affect the signal negatively. In this work, the TR used in the *stand* was 1800 ms and it was shortened to be 240 ms in the *sms8*. The radical TR reduction is one clear explanation for the weaker signal intensity that causes weaker results such as less smooth multifocal maps and smaller t-values. These observations can be seen even with optimal flip angles.

However, the amount of negative effects of using high slice acceleration factors depend on several factors, including reconstruction methods [3, 9, 10], used imaging parameters [3, 72], experimental design and data analysis methods [4, 72]. In addition, the optimal SMS factor is also region dependent [43]. Therefore, characterizing SMS EPI protocols is not straight-forward and balancing between benefits and disadvantages is needed. A shorter TR lowers the signal intensity but also enables a acquisition of a greater number of im-

ages in the same imaging time. This improves the statistical power of fMRI studies due to the increase of the estimated number of independent samples (e.g. degrees of freedom in test statistics) in the data time series [4, 10, 43]. The statistical power of high acceleration factors is seen in the result of this work. Even though the TR of the *sms8* was radically shortened compared to the TR of the *stand* the results of *sms8* were still quite reasonable. The TR used in the *sms8* was 240 ms and in the *stand* 1800 ms. The *sms8* protocol gave clear t-max values in every multifocal region even though they were smaller than the values achieved with the other protocols. In addition, from the multifocal maps of the *sms8* one was able to see which parts of the visual field activate which parts of the brain even though the maps were not as smooth as the maps achieved with the *stand*.

The increase in statistical power is limited by temporal correlations that control the false positive rates [43, 66]. Since SMS EPI sequences enabled the acquisition of a radically greater number of volumes, more complex methods are needed to sufficiently capture temporal correlations [40, 63, 66, 72, 73]. In this work, I used AR(FAST) method implemented into the SPM12 software. The method has potential to improve reliability of fMRI by reducing false positive rates [66, 73]. Since the used SMS EPI protocols produced similar and reasonable results compared to the results of the *stand*, the AR(FAST) method seemed to work well with the data of this study. In general, the used analysis method critically affects to the results of SMS EPI sequences.

Another benefit of accelerated sampling rates is the ability to sample more completely higher frequency signal variations that are unrelated to the BOLD signal changes of the measured task [43]. Signals that are not of interest include cardiac pulsation and changes due to breathing. With standard TRs these signals are typically aliased down to the frequency of the BOLD signal. Shorter TRs enable to either fully sample these high frequency noise signals or more likely to aliase them to a frequency that is not the frequency of the BOLD signal [43]. The separation of high frequency noise signals allows better detection of the task related BOLD signal. Therefore, SMS EPI sequences could increase BOLD sensitivity.

In this work, the *sms2* and the *sms4* protocols produce higher t-max values than the *stand*. With these protocols cluster sizes of t-maxes slightly decreased compared to the *stand* which affects the smoothness of multifocal maps. As an average, the maps achieved with the *stand* were the smoothest but the difference was not big until the slice acceleration factor was more than 4. The measurements to compare the locations of achieved t-max values investigated are there any variation between the locations of the particular t-maxes due false positives. The location of t-maxes varied manly only when slice acceleration factor was brought up to 8. Hence, these results indicate

that moderate slice acceleration factors (*sms2* and *sms4* in this work) might have positive effects to multifocal fMRI. However, although the results are promising, I had only five subjects whose data were acquired with optimised flip angles in this work. Therefore, more measurements with a greater number of subjects are needed to have more reliable results. However, regardless of the flip angles used, the protocols *sms8* and *sms4 GRAPPA2* produced clearly worse results compared to the other protocols.

The results of this work indicates that GRAPPA acceleration factor has negative effects to the data. As an average the protocol *sms2 GRAPPA2* (TR = 720 ms) produced smaller t-score values and cluster sizes, lower SNR and less smooth multifocal maps than the *sms2* (TR = 900 ms) and the *sms4* (TR = 400 ms) whose TR was even shorter. In addition, the results of *sms4 GRAPPA2* (TR = 360 ms) were weaker compared to the results of the *sms4*. However, the TR used in *sms4 GRAPPA2* is shorter than the TR used in *sms4* and therefore the negative effects might be consequence of shortened TR. For further study of the effects of the GRAPPA, it would be better to compare the protocols by using the same TRs. Shorter TRs and the concomitant reductions in flip angles reduce the signal intensity due to the reduced steady state magnetization [3, 43]. Since in the evaluated protocols the TR used significantly varies, it is difficult to say are the negative effects caused by the use of the shortened TR or GRAPPA acceleration.

According to Todd and colleagues, at the periphery of the brain (e.g in V1) the g-factor noise amplification is low due to the accelerated sampling rate [43]. Thus, it is reasonable to use SMS EPI sequences in multifocal fMRI. The results of this Thesis also gave promising results of that moderate slice acceleration factors can be used to improve or accelerate the imaging speed in multifocal fMRI studies. However, the optimal used slice acceleration factor depends always also on the research question.

5.4 Future directions

This work indicates that accelerated sampling rate increases the statistical power in multifocal fMRI. With high slice acceleration factors the single image is worse but the accelerated sampling rate enables to acquire more images in the same imaging time. This compensates the disadvantages of using high slice acceleration factors.

In future studies, it would be interesting to examine more the properties of the used protocols. For example, from the acquired data, it would be interesting to characterize an amount of false positive activation caused by each protocol due to signal leakage between simultaneously excited slices.

Todd and colleagues [9] have investigated the issue from their data and the used analysis method could be applied to the data acquired in this work. In addition, it would be interesting to investigate will the protocols *sms8* and *sms4 GRAPPA2* produce as weak results as in this work if the TR used is not shortened that radically.

In general, SMS EPI is a much investigated imaging method. The obvious benefits for resting-state fMRI are documented by including Preibisch and colleagues [5] and Demetriou and colleagues [4]. Benefits for task fMRI are not as clear and thus more studies are still needed. Since benefits of higher sampling rate depends on several factors including the features of the data analysis, the data acquired in this work can be used to investigate better analysis methods. For example, it would be interesting to examine possible filtering methods that would reduce noise from the accelerated fMRI data. Moreover, simultaneous multi slice imaging is not the only way to accelerate imaging speed and in the future it would be interesting to investigate what other methods we can use to improve and accelerate multifocal fMRI.

Chapter 6

Conclusion

The main focus of this work was to characterize SMS EPI sequence using the multifocal visual stimulation paradigm. With different slice acceleration factors, TR was shortened from 1800 to 240 ms. The evaluated properties were SNR, the value, location and cluster size of maximum t-score and also smoothness and quality of multifocal maps. In addition, the importance of optimised flip angles in accelerated sampling rate and the effects use of simultaneous GRAPPA acceleration on multifocal fMRI data were examined.

This work indicates that moderate acceleration factors with moderate TR reduction can be used to accelerate imaging speed or to increase BOLD sensitivity in multifocal fMRI. Significantly shorter TRs affect data negatively. However, this work shows that even though TR is shortened to 240 ms, t-statistics result in low but significant t-score values and achieved multifocal maps are less smooth but still reasonable. Hence, the optimal slice acceleration factor depends always on the research question. In addition, the results of this work indicate that regardless of the TR used, the use of unoptimised flip angles and simultaneous GRAPPA acceleration factors have negative effects to the SMS EPI data.

Bibliography

[1] S. A. Huettel, A. W. Song, and G. McCarthy. *Functional Magnetic Resonance Imaging*. Sinauer Associates, 2004.

[2] N. K. Logothetis. What we can do and what we cannot do with fMRI. *Nature*, 453(12):869–878, 2008. doi:10.1038/nature06976.

[3] K. Setsompop, B. A. Gagoski, J. R. Polimeni, T. Witzel, V. J. Wedeen, and L. L. Wald. Blipped-controlled aliasing in parallel imaging for simultaneous multislice echo planar imaging with reduced g-factor penalty. *Magnetic Resonance in Medicine*, 67(5):1210–1224, 2012. doi:10.1002/mrm.23097.

[4] L. Demetriou, O. S. Kowalczyk, G. Tyson, T. Bello, R. D. Newbould, and M. B. Wall. A comprehensive evaluation of increasing temporal resolution with multiband-accelerated protocols and effects on statistical outcome measures in fMRI. *NeuroImage*, 176:404–416, 2018. doi:10.1016/j.neuroimage.2018.05.011.

[5] C. Preibisch, J. G. Gastrillon, M. Buhrer, and V. Riedl. Evaluation of multiband EPI acquisition for resting state fMRI. *PLos One*, 10:1–14, 2015. 10.1371/journal.pone.0136961.

[6] S. Ogawa, T. M. Lee, A. R. Kay, and D. W. Tank. Brain magnetic resonance imaging with contrast dependent on blood oxygenation. *Proc. Natl. Acad. Sci. USA*, 87:9868–9872, 1990.

[7] S. Ogawa, D. W. Tank, R. Menon, J. M. Ellermann, and S. G. Kim H. Merkle K. Ugurbil. Intrinsic signal changes accompanying sensory stimulation: functional brain mapping with magnetic resonance imaging. *Proc. Natl. Acad. Sci. USA*, 89(13):5951–5955, 1992. doi:10.1073/pnas.89.13.5951.

[8] K. K. Kwong, J. W. Belliveau, D. A. Chesler, I. E. Goldberg, R. M. Weisskoff, B. P. Poncelet, D. N. Kennedy, B. E. Hoppel, M. S. Cohen,

and R. Turner. Dynamic magnetic resonance imaging of human brain activity during primary sensory stimulation. *Proc. Natl. Acad. Sci. USA*, 89(12):5675–5679, 1992. doi:10.1073/pnas.89.12.5675.

[9] N. Todd, S. Moeller, E. J. Auerbach, E. Yacoub, G. Flandin, and N. Weiskopf. Evaluation of 2D multiband EPI imaging for high-resolution, whole-brain, task-based fMRI studies at 3T: Sensitivity and slice leakage artifacts. *NeuroImage*, 124:32–42, 2016. doi:10.1016/j.neuroimage.2015.08.056.

[10] M. Kiss, P. Hermann, Z. Vidnyanszky, and V. Gail. Reducing task-based fMRI scanning time using simultaneous multislice echo planar imaging. *Neuroradiology*, 60:293–302, 2018. doi:10.1007/s00234-017-1962-4.

[11] L. Henriksson, J. Krvonen, N. Salminen-Vaparanta, H. Railo, and S. Vanni. Retinotopic Maps, Spatial Tuning, and Locations of Human Visual Areas in Surface Coordinates Characterized with Multifocal and Blocked fMRI Designs. *PLoS ONE*, 7(5), 2012. doi:10.1371/journal.pone.0036859.

[12] S. Vanni, L. Henriksson, and A.C. James. Multifocal fMRI mapping of visual cortical areas. *NeuroImage*, 27:95–105, 2005. doi:10.1016/j.neuroimage.2005.01.046.

[13] J. P. Hornak. The basics of MRI, 1996-2019. `https://www.cis.rit.edu/htbooks/mri/inside.htm`. Accessed 10.4.2019.

[14] T. Ethofer, Irina Mader, Uwe Seeger, Gunther Helms, Michael Erb, Wolfgang Grodd, Albert Ludolph, and Uwe Klose. Comparison of Longitudinal Metabolite Relaxation Times in Different Regions of the Human Brain at 1.5 and 3 Tesla. *Magnetic Resonance in Medicine*, 50:1296–1301, 2003. doi:10.1002/mrm.10640.

[15] G. J. Stanisz, E. E. Odrobina, Joseph Pun, Michael Escaravage, S. J. Graham, M. J. Bronskill, and R. M. Henkelman. T1,T2 Relaxation and Magnetization Transfer in Tissue at 3T. *Magnetic Resonance in Medicine*, 54:507–512, 2005. doi:10.1002/mrm.20605.

[16] J. Wang, W. Mao, M. Qiu, M. B. Smith, and R. T. Constable. Factors Influencing Flip Angle Mapping in MRI: RF Pulse Shepe, Slice-Select Gradients, Off-Resonance Excitation, and B_0 Inhomogeneities. *Magnetic Resonance in Medicine*, 56(2):463–468, 2006. doi:10.1002/mrm.20947.

[17] R. R. Ernst and W. A. Anderson. Application of Fourier Transform Spectroscopy to Magnetic Resonance. *The Review of Scientific Instruments*, 37(1):93–102, 1996.

[18] T. C. Mills, D. A. Ortendahl, N. M. Hylton, L. E. Crooks, J. W. Carlson, and L. Kaufman. Partial Flip Angle MR Imaging. *Radiology*, 162(1):531–539, 1987.

[19] R. R. Edelman, P. Wielopolski, and F. Schmitt. Echo-Planar MR imaging. *Radiology*, 192(3):600–612, 1994. doi:10.1148/radiology.192.3.8058920.

[20] R. L. DeLaPaz. Echo-Planar imaging. *RadioGraphics*, 14(5):1045–1058, 1994. doi:10.1148/radiographics.14.5.7991813.

[21] P. Mansfield. Multi-planar image formation using NMR spin echoes. *Journal of Physics C: Solid State Physics*, 10(3):55–58, 1977. doi:10.1088/0022-3719/10/3/004.

[22] R. Rzedzian, P. Mansfield, M. Doyle, D. Guilfoyle, B. Chapman, R. E. Coupland, A. Chrispin, and P. Small. Real-time nuclear magnetic resonance clinical imaging in paediatrics. *Lancet*, 12:1281–1282, 1983.

[23] M. Poustchi-Amin, S. A. Mirowitz, J. J. Brown, R. C. McKinstry, and T. Lin. Principles and Applications of Echo-planar Imaging: A Review for the General Radiologist. *RadioGraphics*, 21(3):767–779, 2001. doi:10.1148/radiographics.21.3.g01ma23767.

[24] A.-R. Mohammadi-Nejad and G.-A. Hossein-Zadeh. Simulation of Echo Planar Imaging in MRI: Application to assessment of field inhomogeneity and chemical shift. *IEEE*, 2008. doi:10.1109/ISSPA.2007.4555485.

[25] D. A. Handwerker, J. Gonzalez-Castillo, M. D'Esposito, and P. A. Bandettini. The continuing challenge of understanding and modeling hemodynamic variation. *NeuroImage*, 62(2):1017–1023, 2012. doi:10.1016/j.neuroimage.2012.02.015.

[26] M. A. Lindquist, Ji Meng Loh, L. Y. Atlas, and T. D. Wager. Modeling the hemodynamic response function in fMRI: Efficiency, bias and mis-modeling. *NeuroImage*, 45(1):S187–S198, 2008. doi:10.1016/j.neuroimage.2008.10.065.

[27] D. A. Feinberg, J. D. Hale, J. C. Watts, L. Kaufman, and A. Mark. Halving MR imaging time by conjugation: demonstration at 3.5 kG. *Radiology*, 161:527–531, 1986.

[28] N.-K. Chen, K. Oshio, and L. P. Panych. Improved Image Reconstruction for Partial Fourier Gradient-Echo Echo-Planar Imaging (EPI). *Magnetic Resonance in Medicine*, 59:916–924, 2008. 10.1002/mrm.21529.

[29] A. Deshmane, V. Gulani, M. A. Griswold, and N. Seiberlich. Parallel MR imaging. *Journal of Magnetic Resonance*, 36(1):55–72, 2012. doi:10.1002/jmri.23639.

[30] K. P. Pruessmann, M. Weiger, M. B. Scheidegger, and P. Boesiger. SENSE: Sensitivity Encoding for Fast MRI. *Magnetic Resonance in Medicine*, 42:952–962, 1999.

[31] M. A. Griswold, P. M. Jakob, R. M. Heidemann, M. Nittka, V. Jellus, J. Wang, B. Kiefer, and A. Haase. Generalized Autocalibrating Partially Parallel Acquisitions (GRAPPA). *Magnetic Resonance in Medicine*, 47:1202–1210, 2002. doi:10.1002/mrm.10171.

[32] M. Blaimer, F. Breuer, M. Mueller, R. M. Heidemann, M. A. Griswold, and P. M. Jakob. SMASH, SENSE, PILS, GRAPPA. How to Choose the Optimal Method. *Top Magn Reson Imaging*, 15(4):223–236, 2004.

[33] D. J. Larkman and R. G. Nunes. Parallel magnetic resonance imaging. *Physics in Medicine Biology*, 52(7):R15–R55, 2007. doi:10.1088/0031-9155/52/7/R01.

[34] H. Lutke, K-D. Merboldt, and J. Frahm. The cost of parallel imaging in functional MRI of the human body. *Magnetic Resonance Imaging*, 24(1):1–5, 2006. doi:10.1016/j.mri.2005.10.028.

[35] S. Muller. Multifrequency Selective RF Pulses for Multislice MR Imaging. *Magnetic Resonance in Medicine*, 6:364–371, 1988.

[36] F. A. Breuer, M. Blaimer, R. M. Heidemann, M. F. Mueller, M. A. Griswold, and P. M. Jakob. Controlled Aliasing in Parallel Imaging Results in Higher Acceleration (CAIPIRINHA)for Multi-Slice Imaging. *Magnetic Resonance in Medicine*, 53:684–691, 2005. doi:10.1002/mrm.20401.

[37] A. A. Maudsley. Multiple-line-scanning spin density imaging. *Journal of Magnetic Resonance*, 41(1):112–126, 1980. doi:10.1016/0022-2364(80)90207-3.

[38] R. G. Nunes, J. V. Hajnal, and D. J. Larkman. Simultaneous slice excitation and reconstruction for single shot EPI. *In Proceedimgs of the 14th Annual meeting of ISMRM, Seatle, Washington, USA*, 2006.

[39] K. Setsompop, S. F. Cauley, and L. L. Wald. Advancing Diffusion MRI Using Simultaneous Multi-Slice Echo Planar Imaging. *MAGNETOM Flash*, 63:16–22, 2015.

[40] A. K. Sahib, K. Mathiak, M. Erb, A. Elshahabi, S. Klamerand, K. Scheffler, N. K Focke, and T. Ethofer. Effect of Temporal Resolution and Serial Autocorrelations in Event-Related Functional MRI. *Magnetic Resonance in Medicine*, 76:1805–1813, 2016. doi.org/10.1002/mrm.26073.

[41] J. Xu, S. Moeller, E. J. Auerbach, J. Strupp, S. M. Smith, D. A. Feinberg, E. Yacoub, and K. Ugurbil. Evaluation of slice accelerations using multiband echo planar imaging at 3T. *NeuroImage*, 83:991–1001, 2013. doi:10.1016/j.neuroimage.2013.07.055.

[42] D. A. Feinberg and K. Setsompop. Ultra-fast MRI of the human brain with simultaneous multi-slice imaging. *Journal of Magnetic Resonance*, 229:90–100, 2013. doi:10.1016/j.jmr.2013.02.002.

[43] N. Todd, O. Josephs, P. Zeidman, G. Flandin, S. Moeller, and N. Weiskopf. Functional Sensitivity of 2D Simultaneous Multi-Slice Echo-Planar Imaging: Effects of Acceleration on g-factor and Physiological Noice. *Fronties in Neuroscience*, 11:1–13, 2017. doi:10.3389/fnins.2017.00158.

[44] D. Purves, G. J. Augustine, D. Fitzpatrick, W. C. Hall, A.-S. LaMantia, J. G. McNamara, and S. M. Williams. *Neuroscience*. Sinauer Associates, 3 edition, 2004.

[45] C. A. Curcio, K. R. Sloan, R. E. Kalina, and A. E. Hendrickson. Human Photoreceptor Topography. *The Journal of Comparative Neurology*, 292:497–523, 1990.

[46] Y. B Saalmann and S. Kastner. Gain control in the visual thalamus during perception and cognition. *Current Opinion in Neurobiology*, 19:408–414, 2009. doi:10.1016/j.conb.2009.05.007.

[47] Questions and answers in MRI. fMRI of visual system. `http://mriquestions.com/visual.html`. Last accessed 8 Sep 2019.

[48] D. C. Van Essen. Organization of Visual Areas in Macaque and Human Cerebral Cortex. *The Visual Neurosciences (L. Chalupa and J. Werner, eds.)*, pages 1–14, 2002.

[49] S. O. Dumoulin and B. A. Wandell. Population receptive field estimates in human visual cortex. *NeuroImage*, 39:647–660, 2009. doi:10.1016/j.neuroimage.2007.09.034.

[50] E. A. DeYoe, G. J. Carman, P. Bandettini, S. Glickman, J. Wieser, R. Cox, D. Miller, and J. Neitz. Mapping striate and extrastriate visual areas in human cerebral cortex. *Proceedings of the National Academy of Sciences of the United States of America*, 93:2382–2386, 1996.

[51] B. A. Wandell, S. O. Dumoulin, and A. A. Brewer. Visual Field Maps in Human Cortex. *NauroImage*, 56:366–383, 2007. 10.1016/j.neuron.2007.10.012.

[52] S. A. Engel, G. H. Glover, and B. A. Wandel. Retinotopic Organization in Human Visual Cortex and the Spatial Precision of Functional MRI. *Cerebral Cortex*, 7(2):181–192, 1997. 10.1093/cercor/7.2.181.

[53] Linda Henriksson. Retinotopic mapping of human visual cortex. `http://ltl.tkk.fi/wiki/RetinotopicMapping`. Last accessed 8 Sep 2019.

[54] A. R. McDowell and D. W. Carmichael. Optimal repetition time reduction for single subject event-related functional magnetic resonance imaging. *Magnetic Resonance in Medicine*, pages 1–8, 2018. doi:10.1002/mrm.27498.

[55] S. Hetzer, T. Midner, T. H. Jochimsen, K. Muller, T. Schlumm, and H. E. Möller. Latency and Echo-Time Dependence of the GRE-BOLD Signal in High-Resolution fMRI. *Proceedings of the 17th Annual Meeting ISMRM, Honolulul Hi, USA*, 17:1609, 2009.

[56] H. Ravi, P. Liu, S-L. Peng, H. Liu, and H. Lu. Simultaneous multislice (SMS)acquisition enhances the sensitivity of hemodynamic mapping using gas challenges. *NMR in Biomedicine*, 29:1511–1518, 2016. doi:10.1002/nbm.3600.

[57] R. M. Weisskoff. Simple Measurement of Scanner Stability for Functional NMR Imaging of Activation in the Brain. *Magnetic Resonance in Medicine*, 36:643–645, 1996.

[58] Wellcome Department of Imaging Neuroscience. Statistical parametric mapping. `https://www.fil.ion.ucl.ac.uk/spm/`. Last accessed 27 May 2019.

[59] J. V. Hajnal, R. Myers, A. Oatridge, J. E. Schwieso, I. R. Young, and G. M. Bydderp. Artifacts due to stimulus-correlated motion in functional imaging of the brain. *Magnetic Resonance in Medicine*, 3:283–291, 1994. doi:10.1002/mrm.1910310307.

[60] K. J. Friston, A. P. Holmes, K. J. Worsley, J.-P. Poline, C. D. Frith, and R. S. J. Frackowiak. Statistical Parametric Maps in Functional Imaging: A General Linear Approach. *Human Brain Mapping*, 2:189–210, 1995.

[61] R. Frackowiak, K. Friston, C. Frith, R. Dolan, C. Price, S. Zeki, J. Ashburner, and W. Penny. *Human Brain Functions*. San Diego: Academic Press, 2 edition, 2004. doi.org/10.1016/B978-0-12-264841-0.X5000-8.

[62] K. J. Friston, D. E. Glaser, R. N. A. Henson, S. Kiebel, C. Phillips, and J. Ashburner. Classical and Bayesian Inference in Neuroimaging: Application. *NeuroImage*, 16(2):484–512, 2002. doi:10.1006/nimg.2002.1091.

[63] S. Bollmann, A. M. Puckett, R. Cunnington, and M. Barth. Serial correlations in single-subject fMRI with sub-second TR. *NeuroImage*, 166:152–166, 2018. doi:10.1016/j.neuroimage.2017.10.043.

[64] A. Eklund, M. Andersson, C. Josephson, M. Johannesson, and H. Knutsson. Does parametric fMRI analysis with SPM yield valid results? An empirical study of 1484 rest datasets. *NeuroImage*, 61(3):565–578, 2012. doi:10.1016/j.neuroimage.2012.03.093.

[65] P. L. Purdon and R. M. Weisskoff. Effect of Temporal Autocorrelation Due to Physiological Noise and Stimulus Paradigm on Voxel-Level False-Positive Rates in fMR. *Human Brain Mapping*, 6(4):239–249, 1998.

[66] N. Corbin, N. Todd, K. Friston, and M. F. Callaghan. Accurate modeling of temporal correlations in rapidly sampled fMRI time series. *Human Brain Mapping*, 39(10):3884–3897, 1994. doi:10.1002/hbm.24218.

[67] K. Uludag, K. Uqurbil, and L. Berliner (Eds.). *fMRI: From Nuclear Spins to Brain Functions*. Springer, 2015.

[68] K. A. Hansen, K. N. Kay, and J. L. Gallant. Topographic Organization in and near Human Visual Area V4. *The Journal of Neuroscience*, 27(44):11896–11911, 2007.

[69] R. A. Poldrack, J. A. Mumford, and T. E. Nichols. *Handbook of Functional MRI Data Analysis*. Cambridge University Press, 2011.

[70] FreeSurfer Software. FreeSurfer. `https://surfer.nmr.mgh.harvard.edu/`. Last accessed 30 Sep 2019.

[71] M. Barth, F. Breuer, P. J. Koopmans, D. G. Norris, and B. A. Poser. Simultaneous Multislice (SMS) Imaging Techniques. *Magnetic Resonance in Medicine*, 75:63–81, 2016. 10.1002/mrm.25897.

[72] J. E. Chen, J. R. Polimeni, S. Bollmann, and G. H. Glover. On the analysis of rapidly sampled fMRI data. *NeuroImage*, 188:807–820, 2019. 10.1016/j.neuroimage.2019.02.008.

[73] W. Olszowy, J. Aston, C. Rua, and G. B. Williams. Accurate autocorrelation modeling substantially improves fMRI reliability. *Nature Communications*, 10:1–11, 2019. 10.1038/s41467-019-09230-w.